ASME Journal of Thermal Science and Engineering Applications
Online journal at:
https://asmedigitalcollection.asme.org/thermalscienceapplication

Impact of Weather Conditions Variability on External Receivers in Real-World Direct Steam Generation Solar Power Tower Plants

Hayder Al-Sarraf[1]
Department of Mechanical Engineering,
Auckland University of Technology,
Auckland 1142, New Zealand;
Midland Refineries Company,
Ministry of Oil, Karbala Refinery,
Karbala 56001, Iraq
e-mail: hayder.al-sarraf@autuni.ac.nz

Ahmed Alhusseny
Department of Mechanical Engineering,
Faculty of Engineering,
University of Kufa,
Najaf 54003, Iraq;
Department of Mechanical and
Aerospace Engineering,
School of Engineering,
University of Manchester,
Manchester M13 9PL, UK
e-mails: ahmedn.alhusseini@uokufa.edu.iq;
ahmed.alhusseny@manchester.ac.uk

Ramon Zamora
Department of Electrical Engineering,
Auckland University of Technology,
Auckland 1010, New Zealand
e-mail: ramon.zamora@aut.ac.nz

Solar power tower plants are promising to decarbonize electricity production, where solar power is concentrated to heat the working heat transfer fluids effectively. However, due to atmospheric effects and cloud cover, such power varies spatially and temporally during the diurnal cycle. Therefore, estimating the net solar thermal power gained by receiver tubes in terms of time and location is highly significant. This research set the foundation for developing the heat irradiance equation as a function of time on external receiver absorbing tubes in the Ivanpah I plant using the SOLARPILOT *tool. Furthermore, a modified Gaussian distribution is derived for the incident heat flux over the tube circumference. Compared to the proposed distribution, it is found that both the uniform and basic Gaussian distributions employed in former computational fluid dynamics simulations would result in about 57.1% overestimation of the total solar power received. Multisegment correlations are also established for the temporal profile of axisymmetric heat flux on each side of the receiver. A thorough thermodynamic analysis procedure is also developed and applied under real-world weather conditions to exhibit the potential of the proposed scheme to handle such complicated computations comprehensively and cost-effectively. Based on the proposed procedure, an in-house* MATLAB *code is built to numerically predict the instantaneous heat losses from the north-facing evaporator panel tubes and their corresponding steam productivity. The results reveal that the onset of nucleate boiling takes up to 2 h from sunrise to reach, with 70% of the tube length required to start evaporation, which lasts to the rest of the tube. However, superheating can be established once solar intensity is strong enough around midday, occupying up to 12.9% of the tube length. The current research has paved the way for future detailed computational fluid dynamics (CFD) investigations of external solar power receivers and has significance in ensuring such systems' reliability and longevity.* [DOI: 10.1115/1.4068836]

Keywords: solar power tower, external receiver, solar irradiance variability, SOLARPILOT, *Ivanpah I plant, direct steam generation, transient thermodynamic analysis*

1 Introduction

Solar energy occupies the leading position among the current sustainable energy resources because of its potential to attain environmental, economic, and safety targets [1]. Annual solar irradiance reaching the earth's surface is estimated at 4 quadrillion kWh [2], which goes beyond the limit that power is needed by the population around the world by more than a hundred times [3]. Even with the abundance and availability of solar irradiance, there is a significant shortcoming in utilizing such irradiance. The low and intermittent density of solar energy due to scattering and attenuation through the atmosphere and cloud events makes it less efficient. Thus, solar irradiance concentrators have emerged to exploit high solar thermal energy [4–6]. Concentrating solar thermal collectors are characterized by a high concentration ratio, meaning that the collector has a much larger surface area than the receiver integrated and can track the sun during the daytime. Plants based on concentrating collectors are called concentrating solar power (CSP) plants. They represent a sophisticated solution to obtain effective solar thermal energy systems, especially in locations characterized by high solar irradiance [7].

Of all current CSPs available nowadays, solar power tower (SPT) plants occupy the leading position in providing high thermodynamic temperatures and efficiency [7,8]. Furthermore, they can be installed in any location worldwide if the direct normal irradiance

[1]Corresponding author.

Manuscript received January 20, 2025; final manuscript received May 16, 2025; published online June 30, 2025. Assoc. Editor: MD Didarul Islam.

magnitude is enough to generate the thermal energy required to run such plants [9]. Such plants consist of hundreds/thousands of mirrors called "heliostats" arranged in circular arrays centered around a solar receiver. The function of heliostats is to receive, reflect, and concentrate the incident solar beam onto the receiver, as shown in Fig. 1. They can supply high levels of concentrated solar power ranging from 200 to 1000 kW/m^2, which would lead to delivering heat transfer fluid (HTF) with a high thermodynamic temperature, hence, maximizing the plant efficiency.

On the other hand, the solar receiver is placed on the top of a tower installed in the center of the SPT plant [10–12]. It is a heat exchanger where the incoming solar thermal power from heliostats is intercepted. Then, this thermal power is absorbed by an HTF that flows inside the tubes through the absorbing tube walls. The thermal power gained by the HTF is then used to run a Rankine cycle turbine and generate electricity. From a geometry point of view, solar receivers are classified into two categories: cavity and external receivers. The two types of solar receivers have been employed in solar power tower plants worldwide. Nevertheless, the external receiver has several characteristics that outperform the cavity one, including simplicity in configuration, transportation, and maintenance [13], and about 25% less absorbing area required to harvest the same thermal irradiance [13]. However, the literature shows that external receivers have not been investigated as much as cavity ones despite their above-mentioned merits [14]. In direct steam generation (DSG) technology, water can vaporize directly while flowing inside the receiver tubes. Thus, it has drawn high attention due to the following advantages: less complex plant design, higher thermodynamic temperature, higher thermal efficiency, and reduction in initial cost [15–17].

Weather conditions have a direct impact on SPT receivers' performance. As the solar irradiance varies during the day, the heat flux reflected by heliostats is variable accordingly. Such variation directly impacts the operation and performance of SPT plants. For instance, a significant part of the solar thermal power could be blocked when cloud cover occurs. Consequently, the electric power delivered to the grid decreases. This problem adversely affects grid reliability, stability, and even operators, who are responsible for balancing the demand and supply of electric power. Other key weather conditions that simultaneously affect the SPT receiver's performance are the ambient temperature and wind speed variations, which characterize thermal losses. Therefore, increasing attention has been paid to investigating the thermal performance of external receivers, considering the effect of wind speed and direction on radiative and convective heat losses. Rodríguez-Sánchez et al. [18] investigated the hydrodynamical, thermal, and mechanical impact of using molten salt in external tubular receivers of SPT plants, taking into consideration the variation in tube wall temperature both in circumferential and axial directions. Thermal losses from radiation were higher than those reported in the literature, with lower receiver thermal efficiency. This finding has been attributed to the higher effective tube temperature than the mean wall temperature of the tube rear on thermal radiation. However, the results were based on an averaged value for the maximum heat flux applied rather than considering a transient heat flux. In a related context, various flow patterns of molten salt-cooled external receivers used in solar power towers have been analyzed and simulated by Rodríguez-Sánchez et al. [19], where both single and multiple flow patterns have been investigated under the assumption of clear sky conditions. It was found that optimal performance can be achieved with a receiver without a crossover only under high solar flux, unlike one with a crossover, which can perform well even under a lower rate of incident solar irradiance. It was also stated that the orientation of HTF flow paths in the external receiver plays a crucial role in improving its availability and reliability. Furthermore, it was found that among the operating conditions affecting the performance of SPT plants, the direct normal irradiance (DNI) and the solar elevation directly impact the start-up and shutdown operations. However, the authors have not considered the transient state of DNI during the daytime, where a single DNI value at the solar noon of the spring equinox has only been adopted in their analysis. In addition, Liu et al. [20] proposed novel tubes for molten salt solar receivers to alleviate the nonuniform heat distribution. They found that the temperature variations in the circumference are lower compared to traditional solar receiver tubes. In the numerical analysis presented by Crespi et al. [21], the performance of a molten salt-cooled SPT plant utilizing thermal energy storage systems has been investigated under solar irradiance fluctuation due to cloud cover. The influence of different types of clouds has been considered to identify the most efficient aiming strategy to be more uniform in the distribution of heat flux on the receiver surface. It was found that a total shadow results in the worst operation conditions compared to a partial one due to smaller clouds passing over the solar field. However, only three hours (9:00, 12:00, and 15:00) have been considered for the analysis in the spring equinox, summer, and winter solstice. A transient model was developed by Cagnoli et al. [22] for computational fluid dynamics (CFD) analysis of the impact of wind speed and direction on the performance of the sodium-cooled external receiver in the Jemalong Solar Thermal Station plant as a reference plant [23]. Such a transient CFD model is considered pioneering to simulate the short-term heat fluctuation due to cloud cover and its influence on receiver performance. Even though a detailed simulation has been presented, the instantaneous effects due to temporal variation in DNI magnitude have not been considered, where only specific time intervals for clouds to pass over the solar field have been considered for the simulation. Qaisrani et al. [24] numerically analyzed the thermal performance and efficiency of the water-cooled external tubular receiver under different wind speeds and directions. However, the analysis was carried out for only a maximum heat flux of 425 kW/m^2 applied at the center of the receiver tube facing the north side. Four wind velocities (3, 6, 9, and 12 m/s) and six wind directions have been tested. Results showed that external receiver efficiency lies in the range of 71–77%, depending on the wind velocity. A similar numerical analysis was also conducted by Qaisrani et al. [13] to investigate the effect of wind speed and direction on the thermal performance of external but rectangular receivers. It was found that increasing wind velocity increases convective heat losses regardless of its direction. They also found that adding a blocking-wind wall on the receiver can reduce the convective heat losses, where for a wind velocity of 9 m/s that is normal to the receiver's face, the heat losses are reduced by 33% when a 1m-width block is used compared to 29% reduction when its width is reduced to 0.75 m.

Another issue found in the literature based on CFD simulation is how the incident radiation heat flux is distributed over the outer surface of the HTF tube. Some researchers have considered a uniform distribution over the tube perimeter [25]. In practice, such approximation is, however, unfeasible due to the imbalance between the thermal energy carried by solar radiation and that available to harvest as a solar beam normal to the tube wall. Another approach has been adopted that follows a Gaussian distribution for the incident solar heat flux [24–27], but with a peak value that satisfies the overall solar power offered in the precedent approach for uniform heat flux. Therefore, it also causes an overestimation of the solar thermal power available to be gained from the HTF tube. For instance, Maytorena and Hinojosa [25] numerically investigated the DSG in vertical tubes exposed to concentrated solar power. The investigation based on the Gaussian distribution of incident heat flux indicates that either a decrease in mass flux by 44% or an increase in heat flux applied by 40% increases steam production by more than four times. In a related context, another CFD analysis has been conducted by Maytorena et al. [28] to numerically examine the effects of tube wall thickness and longitudinal rectangular internal fins on the thermal performance of water-cooled tubular receivers. It was found that placing longitudinal fins significantly reduces the tube surface temperature on the irradiated side and enhances heat transfer to the water. The same authors have further extended the last two pieces of research to investigate the thermal and mechanical performance of solar receivers employing

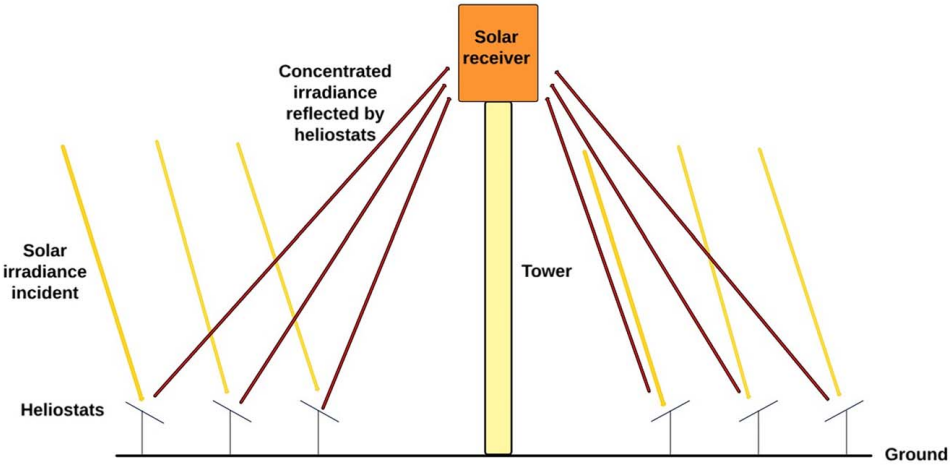

Fig. 1 A schematic representation of the solar tower and heliostats in the SPT plant

DSG technology in SPT plants [29]. The best performance was found for a tube configuration with 3 mm thickness in the receiving surface region and 5 mm thickness in the adiabatic surface region. Hence, in such a configuration, the maximum temperature gradients, temperature, and maximum stresses could be decreased by 31%, 14%, and 38%, respectively.

As previously mentioned, SPT plants consist of numerous sun-tracking mirrors called heliostats to concentrate and reflect the incident sun rays onto the receiver. Such optically complex technology makes it too hard to optimize during the design stage or simulate while operating for further development in the future. Therefore, several tools have been developed to simulate the distribution of concentrated sunrays incident on SPT receivers. For instance, a recent software called the FLUXSPT tool has been developed by Sánchez-González et al. [30] to characterize the heliostat field and flux mapping on receiver absorbing tubes. It employs the convolution-projection method, in which the solar flux distribution is projected from the image plane onto the tubes of solar receiver panels. However, the FLUXSPT tool cannot accommodate more than one specific DNI measurement. Also, its application is restricted to only cylindrical-shaped external receivers and for a limited number of solar power tower plants: Shouhang Dunhuang Phase I, Gemasolar Thermosolar, and Crescent Dunes [23]. Another similar tool is the open-source SOLARPILOT software [31] developed by the National Renewable Energy Laboratory (NREL). Unlike the FLUXSPT tool, SOLARPILOT can cover all characteristics present in any SPT plant and return the required data. It can also accommodate more than one specific DNI value at a time, making it capable of predicting the transient heat flux distribution over an SPT receiver during the daytime. This is why the SOLARPILOT software has received increasing attention during the design and operation of SPT plants. For example, the numerical analysis conducted by Qaisrani et al. [24] determines the thermal efficiency and performance of a water-cooled external tubular receiver under different wind speeds and directions. It was found that the maximum value of incident heat flux is located at the center of the receiver side facing north. However, this research still needs extension to consider the influence of the temporal variation of heat flux during the diurnal cycle. The SOLARPILOT was also employed to examine further the impact of the wind environment on the thermal performance of an external rectangular receiver by Qaisrani et al. [13]. However, only the receiver's north side has been considered, ignoring the influence of the remaining sides (east, west, and south) on the receiver's thermal performance. In addition, considering that only a single DNI value for the analysis is not enough to estimate the receiver's performance, the analysis should be extended to include several values of DNI during the daytime. More recent studies have also employed the SOLARPILOT software in a variety of relevant applications, such as the design of a modular combined power SPT plant integrated into a gas turbine cycle with a direct thermal storage system [32], structural

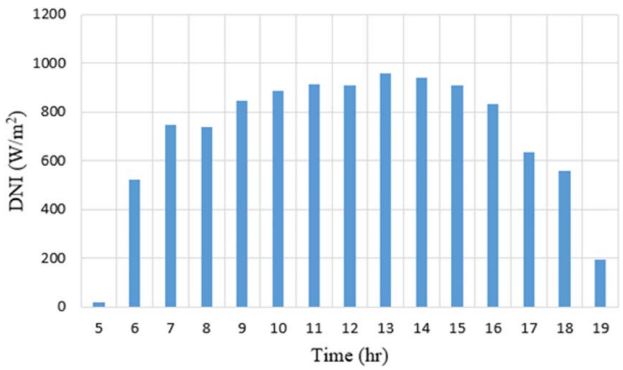

Fig. 2 Hourly averaged DNI measurements on June 21, 2015, at the University of Nevada, Las Vegas, USA [36]

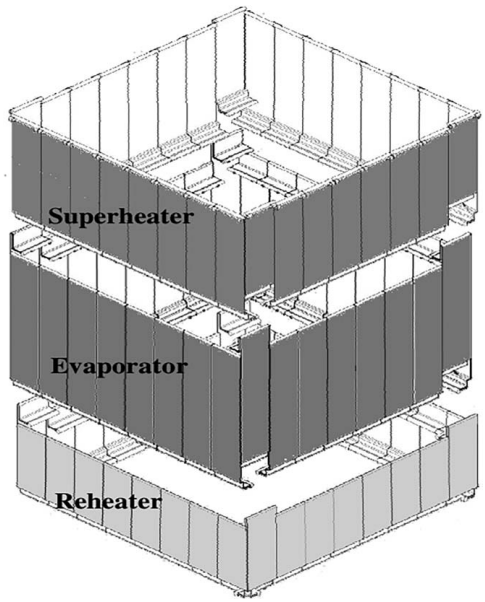

Fig. 3 The external rectangular receiver configuration in ISEGS [38]

Table 1 The length, diameter, and number of panels for the three receiver sections

Receiver section	Tube		No. panels	Tubes/panel
	Length (m)	Diameter (mm)		
Evaporator	10.4	25.4	32	70
Superheater	8.5	19.05	32	90
Reheater	4.9	38.1	32	46

evaluation of a molten salt-cooled SPT receiver operating at a high temperature exceeding 700 °C [33], determination of suitable regions for particle heating receiver SPT plants in the Middle East and North Africa [34], optimization of using SPT in low-to-medium-temperature heat processes for use in industrial applications [35].

Despite the performance and economic advantages of integrating external receivers with DSG compared to cavity receivers and/or molten salt-based plants, the literature reveals a lack of research focusing on this promising combination. Moreover, the impact of solar irradiance fluctuations and real atmospheric conditions on steam generation in SPT plant receivers has not been investigated yet. Above all, considering the large scale and complexity of SPT plants, the available simulation methods for analyzing the performance of SPT are either too complicated and expensive or limited. Therefore, the current research is dedicated to bridging such knowledge gaps by introducing a simplified yet sufficiently comprehensive procedure to predict the net heat flux and daytime-varying steam productivity of DSG external solar receivers under real-world weather conditions. By doing so, electric power produced by the turbine-generator system can be easily computed considering off-design factors (solar irradiance and weather fluctuations), which, to the best of the authors' knowledge, have not been addressed before.

2 Mathematical Modeling

2.1 Problem Description. In this research, the Ivanpah Solar Electric Generating System (ISEGS) CSP Project at Primm, Nevada/California border, USA [23], was taken as a reference plant for two reasons. First, this plant employs an external rectangular receiver module, which is the point of interest during the current research. Second, it represents one of the most recent operational SPT plants worldwide, operating since 2014. On the other hand, the hourly averaged DNI surface measurements required for research on a particular day of the year can be obtained from the Measurement and Instrumentation Data Center (MIDC) [36] by NREL. The NREL website [37] provides an extensive database of meteorological information spanning various locations in the United States, with remarkable precision. The summer solstice day, June 21, 2015, is selected for the ongoing research, where DNI measurements are obtained from an NREL station close to the Ivanpah solar thermal power plant (48.6 miles), University of Nevada, Las Vegas [36], as shown in Fig. 2. The geographical data of the Ivanpah plant are latitude: 36.107 north, longitude: 115.1425 west, elevation: 615 m AMSL, and Universal Time Coordinated (UTC-7).

The ISEGS plant consists of three units with a total capacity of 392-MW gross (377-MW net), where Ivanpah I produces 126 MW while Ivanpah II and III produce 133 MW each. The heliostats field includes 173,500 mirrors, with 53,500 heliostats in Ivanpah I and 60,000 heliostats in each of Ivanpah II and III, and each heliostat has an aperture area of 15 m^2. The tower height is 140 m for each unit. The current research only considers Ivanpah I since all units share the same operational concepts and conditions, except that Ivanpah II and III produce slightly higher power. The solar receiver is a rectangular-shaped external receiver comprising three sections: evaporator, superheater, and reheater, as shown in Fig. 3 [38]. The receiver is characterized by a 23.8-m total height and 256-m^2 square base, and each side consists of eight panels, with a 2-m width per panel. Further details regarding the tubes' length and diameter of the three receiver sections are illustrated in Table 1. It is worth mentioning that the current research is dedicated to investigating the evaporator section only. The subcooled water enters the evaporator section from the bottom through the main headers and is then distributed evenly among the evaporator tubes. Then, it leaves the evaporator section either as subcooled water, saturated steam, or superheated steam, depending on how intense the solar irradiance is during the daytime.

2.2 Assumptions. Several considerations have been adopted to reduce the complexity of the current problem as follows:

(1) Instantaneous DNI incident is the same for the whole heliostat field.
(2) The water flowrate is distributed evenly among each receiver section.
(3) For the evaporator section, only one absorbing tube from each side is considered for computational analysis due to the similarity in flow configuration between the tubes of each section.
(4) One remedy to reduce the problem size is to follow an axisymmetric approximation for the transport phenomena involved. This demands a uniform heat flux applied all over the perimeter of the HTF tube under consideration. However, the rear half of the HTF tube is thermally insulated, while the front one is not evenly heated, as shown in Fig. 4.

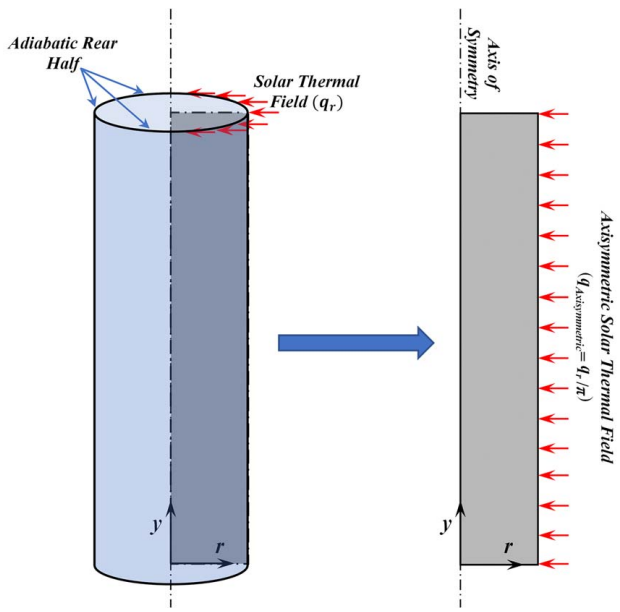

Fig. 4 Converting the three-dimensional problem to a simplified two-dimensional axisymmetric one

So, further treatment is introduced in the next sections to apply such approximation to a greater extent of realism and ensure that only the effective solar thermal power is applied uniformly over the tube circumference.

(5) The thermal resistance of the tube wall is very small and can be neglected.
(6) The transport phenomena involved are considered one-dimensional, ignoring any changes in the radial direction, i.e., only bulk changes have been considered along the axial direction of the tube.
(7) The heat gain processes involved have been assumed to be quasi-transient. In other words, only transient influence has been considered due to temporal variation in solar heat gain.
(8) Depending on the working fluid phase (subcooled liquid, wet steam, superheated vapor), its thermal properties, except the specific heat, are considered constant with values referenced to the threshold temperature of each state. Accordingly, thermophysical properties of water that directly influence the determination of single-phase heat transfer coefficient for each heating process involved are considered constant over that stage. This assumption is based on precalculations conducted to examine the sensitivity of the computed heat transfer coefficient to the temperature change over each heating stage. It has been found that changes in thermophysical properties due to temperature variation do not significantly influence the value of the single-phase heat transfer coefficient computed for any heating stages. On the other hand, the specific heat is dealt with as a temperature-dependent property because the computed values of the instantaneous and local bulk temperature are too sensitive to its change with temperature.

2.3 Governing Equations and Boundary Conditions. The governing equations adopted in the current thermodynamic analysis are based on the mass and energy conservation principles, considering transient behavior and one-dimensional geometry. Accordingly, thermal energy conservation is implemented based on a control volume of the HTF tube as follows:

$$\frac{dH_{\mathrm{HTF}}}{dt} = \sum_{w} Q \rightarrow \frac{\Delta H_j}{\Delta t} = Q_{w,\mathrm{net}_j} \tag{1}$$

For sensible heating, the above equation can be written as

$$\dot{m}\ \mathrm{cp}\ \Delta T_{b_j} = q_{\mathrm{net}_j} A_{s,\mathrm{out}} \tag{2a}$$

While for latent heating, it becomes

$$\dot{m} L_{fg}\ \Delta x_j = q_{\mathrm{net}_j} A_{s,\ \mathrm{out}} \tag{2b}$$

The tube's outer surface is subject to a transient wall heat flux q_w reflected by the heliostats field. However, a fraction of this concentrated heat flux is lost due to convective and radiative heat exchange with the colder surrounding ambient. Therefore, the net wall heat flux gained by the tube can be expressed as

$$q_{\mathrm{net}} = q_w - \ q_{\mathrm{conv}} - q_{\mathrm{rad}} \tag{3}$$

where q_{conv} and q_{rad} stand for thermal losses due to convection and radiation heat exchange with the ambient.

Depending on the water phase at each discrete section, up to three distinct heating mechanisms can occur inside the tube. First, sensible heating dominates in the subcooled section. Next, if the solar irradiance is high enough to let the water vaporize, the evaporation latent heating dominates. As the heat flux continues to increase, sensible heating may re-prevail, establishing a superheating region at the end of the tube. Accordingly, for sensible heating processes within the evaporator section, the following equations are to be used in order:

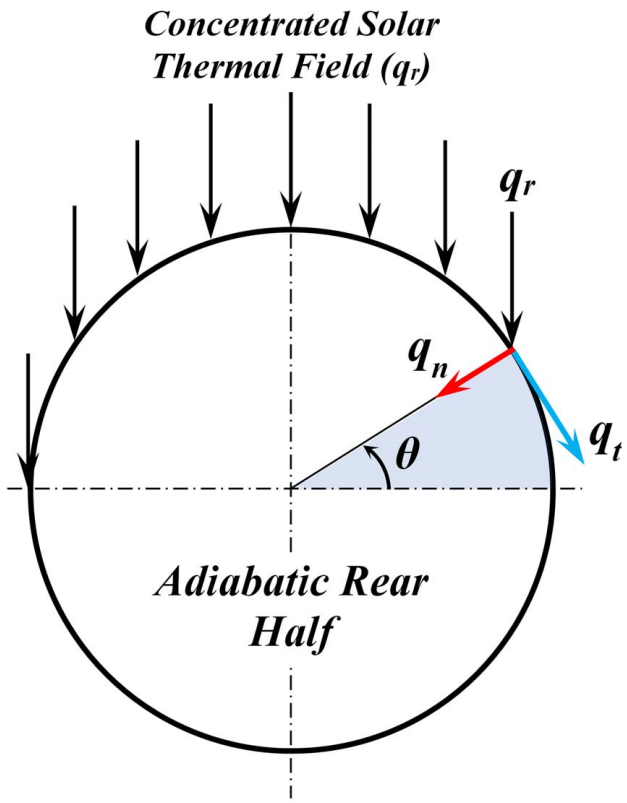

Fig. 5 Concentrated solar power (q_r) components on a receiver tube

$$\mathrm{Re}_i = \frac{4\dot{m}}{\pi d \mu_i} \tag{4}$$

$$h_i = 0.023 \frac{k_i}{d} \mathrm{Re}_i^{0.8} \mathrm{Pr}_i^{1/3} \tag{5}$$

where (i) indicates the water condition at the beginning of the subcooled or superheated section:

$$\dot{m}\mathrm{cp}(T_{\mathrm{ex}} - T_{\mathrm{in}}) = q_{\mathrm{net}} A_{s,\mathrm{out}} \tag{6}$$

$$T_b = \frac{T_{\mathrm{in}} + T_{\mathrm{ex}}}{2} \tag{7}$$

$$h_i A_{s,\mathrm{in}} (T_w - T_b) = q_{\mathrm{net}} A_{s,\mathrm{out}} \tag{8}$$

For the latent heating process, the increase in the vapor fraction generated per unit length within the boiling region of the evaporator section can be computed from the heat balance as follows:

$$\dot{m}\ L_{fg} \Delta x = q_{\mathrm{net}} (\pi D \Delta y) \tag{9}$$

By integration over a particular section:

$$x = \frac{\pi D q_{\mathrm{net}}}{\dot{m} L_{fg}} y \tag{10}$$

As the objective of the current analysis is to present a simplified but accurate enough one-dimensional thermodynamic analysis, the model developed by Kandlikar [39] for predicting saturated flow boiling heat transfer coefficient inside stainless steel or copper heated tubes, has been employed due to its predictive ability for different working fluids, including water. This model can effectively represent the dependence of the two-phase flow heat transfer

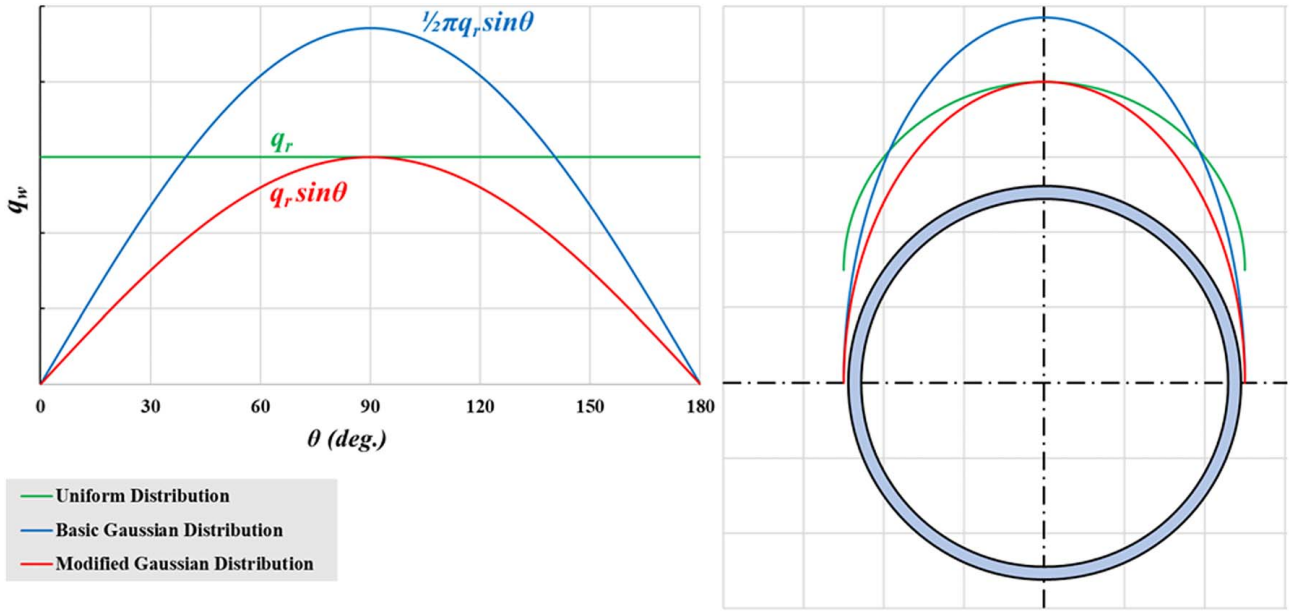

Fig. 6 Modified Gaussian distribution compared to the uniform and basic Gaussian distributions

coefficient (h_{TP}) on the vapor quality (x), mass flux (G), and net wall heat flux (q_{net}) as follows [39]:

$$h_{TP} = \max(h_{nbd}, h_{cbd}) \tag{11}$$

Where the nucleate boiling dominant (h_{nbd}), and convection boiling dominant (h_{cbd}) can be estimated as [39]

$$h_{nbd} = (1-x)^{0.8}\, h_l[0.6683\ \mathrm{CO}^{-0.2} + 1058\ \mathrm{BOLG}^{0.7}F] \tag{12a}$$

$$h_{cbd} = (1-x)^{0.8} h_l[1.136\ \mathrm{CO}^{-0.9} + 667.2\ \mathrm{BOLG}^{0.7}F] \tag{12b}$$

where F represents a fluid-surface combination factor equal to 1 for water as a working fluid [39], while

$$\mathrm{CO} = \left(\frac{1-x}{x}\right)^{0.8}\left(\frac{\rho_v}{\rho_l}\right)^{0.5} \tag{12c}$$

$$\mathrm{BOLG} = \frac{q_{net}}{L_{fg}G} \tag{12d}$$

$$h_{TP}A_{s,in}(T_w - T_{sat}) = q_{net}A_{s,out} \tag{13}$$

To close the mathematical model, two boundary conditions are required. The first is the hydraulic and thermal conditions at the evaporator section inlet, where subcooled water at 160 bar and 460 K flows into the evaporator with a (0.046875 kg/s) mass flow-rate per tube. The second one is the thermal boundary condition at the tube wall, which is subject to a transient heat flux q_w. However, only a fraction of that flux participates in the heating phenomena due to the convective and radiative heat losses, which are computed as follows:

$$q_{conv} = h_{out}(T_w - T_{amb}) \tag{14}$$

$$q_{rad} = \sigma\varepsilon(T_w^4 - T_{sky}^4) \tag{15}$$

It is worth noting that those heat loss modes are locally and temporally changing for two reasons. The first is due to the local increase in wall temperature (T_w) along the tube, while the other is due to the transient nature of both the wall and the ambient temperature (T_{amb}). The temporal change of the latter can be computed using relevant weather data [36] correlated as follows:

$$T_{amb}(K) = 305.65 - 1.448\times10^{-5}t + 9.09\times10^{-8}t^2 - 5.564\times10^{-12}t^3 + 1.82\times10^{-16}t^4 - 2.86\times10^{-21}t^5 + 1.693\times10^{-27}t^6 \tag{16}$$

The transient change in sky temperature (T_{sky}) can, on the other hand, be approximated as [40]

$$T_{sky}(K) = 0.0522(T_{amb}(K))^{3/2} \tag{17}$$

While the tube's outer surface emissivity (ε) is 0.86 [41].

Eventually, the convective heat losses from the tube's outer surface are attributed to two components, forced and natural convection, and could be estimated as [42]

$$h_{out} = (h_{nat}^3 + h_{for}^3)^{1/3} \tag{18}$$

Therefore, it is necessary to quantify the role played by each component relative to the other using a simplified scale analysis based on the order of magnitude of the Richardson number (Ri):

$$\mathrm{Ri} = \frac{natural\ convection}{forced\ convection} = \frac{\mathrm{Gr}}{\mathrm{Re}^2} = \frac{g\beta\Delta TL^3/\nu^2}{(UD/\nu)^2} = \frac{g\beta\Delta TL^3}{U^2D^2} \tag{19a}$$

Then, the order of magnitude for the ratio of natural to forced convection role can be expressed as

$$O(\mathrm{Ri}) = \frac{O(g)O(\beta)O(\Delta T)O(L^3)}{O(U^2)O(D^2)} \tag{19b}$$

Knowing that the order of magnitude (O) of the above parameters can be estimated as

$$O(g)\sim10^1,\ O(\beta)\sim10^{-3},\ O(\Delta T)\sim10^2,\ O(L)\sim10^1,\ O(U)\sim10^1,\ O(D)\sim10^{-2}$$

Thus,

$$O(\mathrm{Ri}) \sim \frac{10^1\times10^{-3}\times10^2\times(10^1)^3}{(10^1)^2\times(10^{-2})^2} \sim 10^5 \gg 1 \tag{19c}$$

Hence, natural convection dominates and overwhelms the role played by the other component. Accordingly, the analysis simplifies

Fig. 7 Aerial image of Ivanpah I, CA, USA

significantly by ignoring the forced convection compared to the natural one without risking the accuracy of the procedure planned. Consequently, the heat transfer coefficient over the tube's outer surface can be approximated following the correlation established by Al-Arabi and Khamis [43] for natural convection over vertically oriented slender cylinders, as follows:

$$h_{\text{out}} = 0.47 \frac{k_{\text{air}}}{L} \frac{(Gr_L Pr)^{1/3}}{(Gr_D)^{1/12}} \tag{20}$$

2.4 Approximations Used to Estimate Heat Flux in Thermal Analysis of Solar Power Tower Receivers. As previously mentioned, each side of the SPT receiver sections consists of 8 panels with several tubes, not to mention the transient phenomena involved due to the temporal variation in the solar heat flux received during daytime. Hence, considering all the HTF tubes in CFD simulation or thermodynamic analysis of SPT receivers is quite complex and costly. Therefore, due to the periodicity and similarity of the tubes, only a single tube can be considered for simulating each side and section of the receiver, as mentioned in the assumptions. This would significantly reduce the size of the solution grid required, leading to significant savings in the computational cost and time anticipated for performing the subsequent simulation processes. To this end, each receiver side's total solar power incident is divided by its total area to compute the average heat flux (q_r) imposed on receiver panels at specific times. However, only the front half of the absorbing tube receives a solar beam reflected from heliostats. Furthermore, such incident solar power has an ineffective irradiance beam form over the whole tube wall [44]. This is due to the curvature of the tube wall in the circumferential direction, resulting in the dissipation of solar rays tangent to its outer surface, as shown in Fig. 5. Therefore, special attention should be paid to this issue to ensure that the distribution of incident solar flux makes sense and meets the principle of energy conservation.

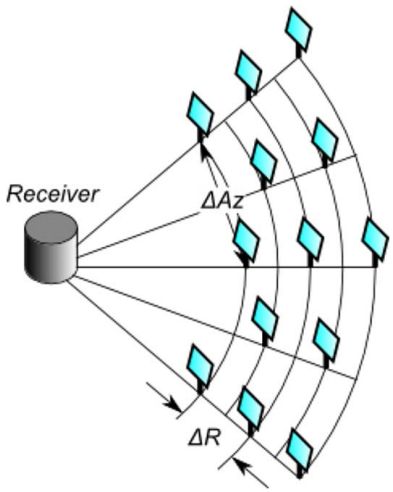

Fig. 8 Heliostats layout based on the Radial Stagger method [48]

2.4.1 Approximation for Three-Dimensional Analysis. As Fig. 5 depicts the solar beam component (q_w) that is normal on the tube wall can be computed following a modified Gaussian distribution as follows [45]:

$$q_w = q_n = q_r \sin\theta, \ (0 \le \theta \le \pi) \tag{21}$$

The total solar power incident on the tube wall (Q_T) can be computed as [44]

$$Q_T = \int_{A_s} q_w dA = \left| \int_0^{\pi} q_w r_0 d\theta \right| = q_r r_0 \left| \int_0^{\pi} \sin\theta d\theta \right| = 2 q_r r_0 \tag{22}$$

As preceded, two other approximations have been employed in the CFD simulation of SPT receivers. The first assumes a uniform

distribution of heat flux over the heated surface of the HTF tube, considering the average value of incident solar flux on the receiver panels, i.e., $q_w = q_r$, resulting in an overall solar power received of $Q_T = \pi q_r r_o$. The other approach adopts a basic Gaussian distribution, $q_w = q_{\max}\sin\theta$, with a peak value ($q_{\max}$) that satisfies the overall solar power offered in the approach of uniform heat flux as follows:

$$Q_T = q_{\max}\, r_o \left| \int_0^{\pi} \sin\theta \mathrm{d}\theta \right| = 2q_{\max} r_o = \pi q_r r_o \Rightarrow q_{\max} = \frac{\pi}{2} q_r \quad (23)$$

Thus,

$$q_w = \frac{\pi}{2} q_r \sin\theta \quad (24)$$

Accordingly, when a uniform distribution is assumed around the tube wall, as it is in some CFD analysis [25], an $(1/\sin\theta) - 1$ error would exist while estimating the local solar radiation flux imposed on the tube wall. This, in turn, results in an 57.1% overestimation of the HTF tube's total solar power received per meter length. Similar heat flux overestimation also exists even in other CFD investigations that follow the basic Gaussian distribution [25,27,44,45] for the reasons mentioned earlier. The difference between the above-mentioned three approaches can be better summarized in Fig. 6.

2.4.2 Approximation for Axisymmetric Thermodynamic or Computational Fluid Dynamics Analysis. One remedy to reduce the size of the problem to deal with in thermodynamic analysis or CFD simulation of SPT receivers is to follow an axisymmetric approximation for the transport phenomena involved. This demands a uniform heat flux applied all over the perimeter of the HTF tube. However, the rear half of the HTF tube is thermally insulated, while the front one is not evenly heated due to the above-mentioned reasons. So, to apply such approximation to a higher extent of realism, the total solar power incident on the tube wall, i.e., $Q_T = 2q_r r_o$ as Eq. (23) suggests, should be divided by the tube perimeter, as shown in Fig. 4, to ensure that only the effective solar thermal power is applied uniformly over the tube circumference as follows:

$$q_{Axisymmetric} = \frac{Q_T}{2\pi\, r_o} = \frac{q_r}{\pi} \quad (25)$$

3 Simulation Procedure

3.1 SOLARPILOT Simulation. The NREL open-source "SOLARPILOT" software [31] based on the Monte-Carlo ray tracing method [46] considering the following assumptions, has been employed to accurately detect heat flux profiles on the solar receiver absorbing tubes. SOLARPILOT depends upon weather files and atmospheric conditions for every location. The meteorological data were collected from the National Solar Radiation Database (NSRDB) [47] because SOLARPILOT does not have a weather file corresponding to the Ivanpah plant location. The weather file collected serves as the foundation of optimization if the weather file is selected as the insolation model. The sun's position is determined based on the location specified in the weather file.

Details of the models adopted for sun shape, insolation, and atmospheric attenuation were specified in the climate part of SOLARPILOT. Design point definition, design values, field boundaries, and field configuration are then set using the layout setup panel of the SOLARPILOT. The Solar Field Design Power, which, on the other hand, represents the total power supplied to an HTF circulating inside the receiver absorbing tubes, can be thought of as the power provided by heliostats minus the convective, emissive, and reflective losses. However, the losses due to convection and radiation are functions of the tube wall temperature, which is locally variable depending on several factors. Therefore, those two components have been zeroed to only predict the concentrated

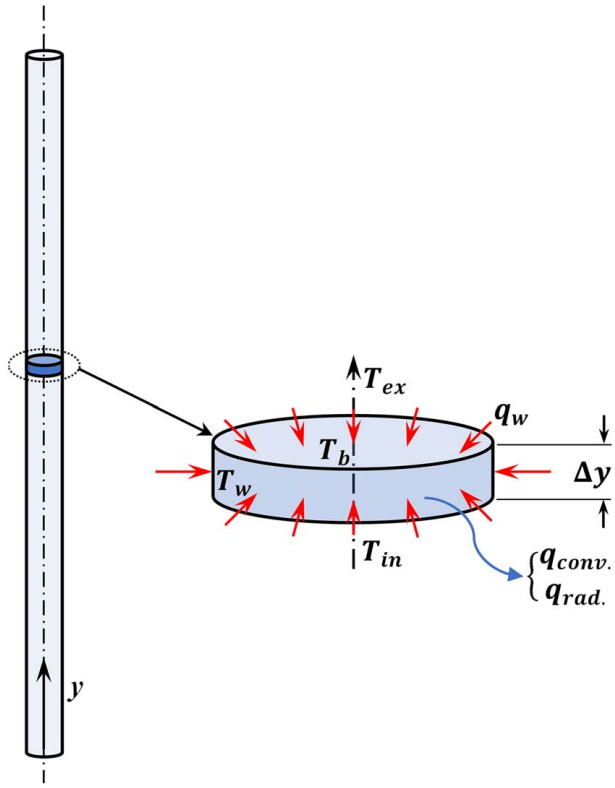

Fig. 9 Representation of solution element with its typical boundary conditions

solar power incident on the receiver minus the reflective component as follows:

$$\dot{Q}_w = (1-\alpha)\dot{Q}_{\mathrm{inc}} \quad (26)$$

The excluded losses, however, will be accounted for later when performing a detailed hydro-thermodynamic analysis, as the tube wall temperature will be available then.

To set up the actual land boundaries of Ivanpah I in CA, USA, the Google Earth tool is used to create a land boundary array as shown in Fig. 7. Hence, the gray area represents the whole land of the plant. The four diagonal green lines and the circular path are the main roads in the plant. The red area in the middle signals the power block, and the yellow pin identifies the location of the solar tower. By doing so, placing any potential heliostat in the exclusion areas can be avoided.

Then, the design characteristics of the Ivanpah I plant have been specified. Those include the actual optical height (140 m), while the Radial Stagger is used as a layout method in which heliostats are mounted alternatively on iso-azimuthal paths at constant radii, as shown in Fig. 8. In addition, adopting the Radial Stagger spacing method eliminates blocking to ensure the irradiance reflected is not blocked by neighboring heliostats from reaching the solar receiver.

The heliostats' optical characteristics have also been set, including their geometry, focus parameters, optical error parameters, and mirror performance parameters. Two rows of mirrors form each heliostat, and each row includes six identical facets, where the dimensions of every heliostat are 4.2 m wide and 3.2 m high [49]. The Heliostat canting method is on-axis at slant option to aim the concentrated irradiance at the solar receiver. Furthermore, for the heliostat focusing strategy, the focal distance has been set equal to the distance between the solar receiver center and the heliostat pivot spot to focus on the incident irradiance on the receiver center.

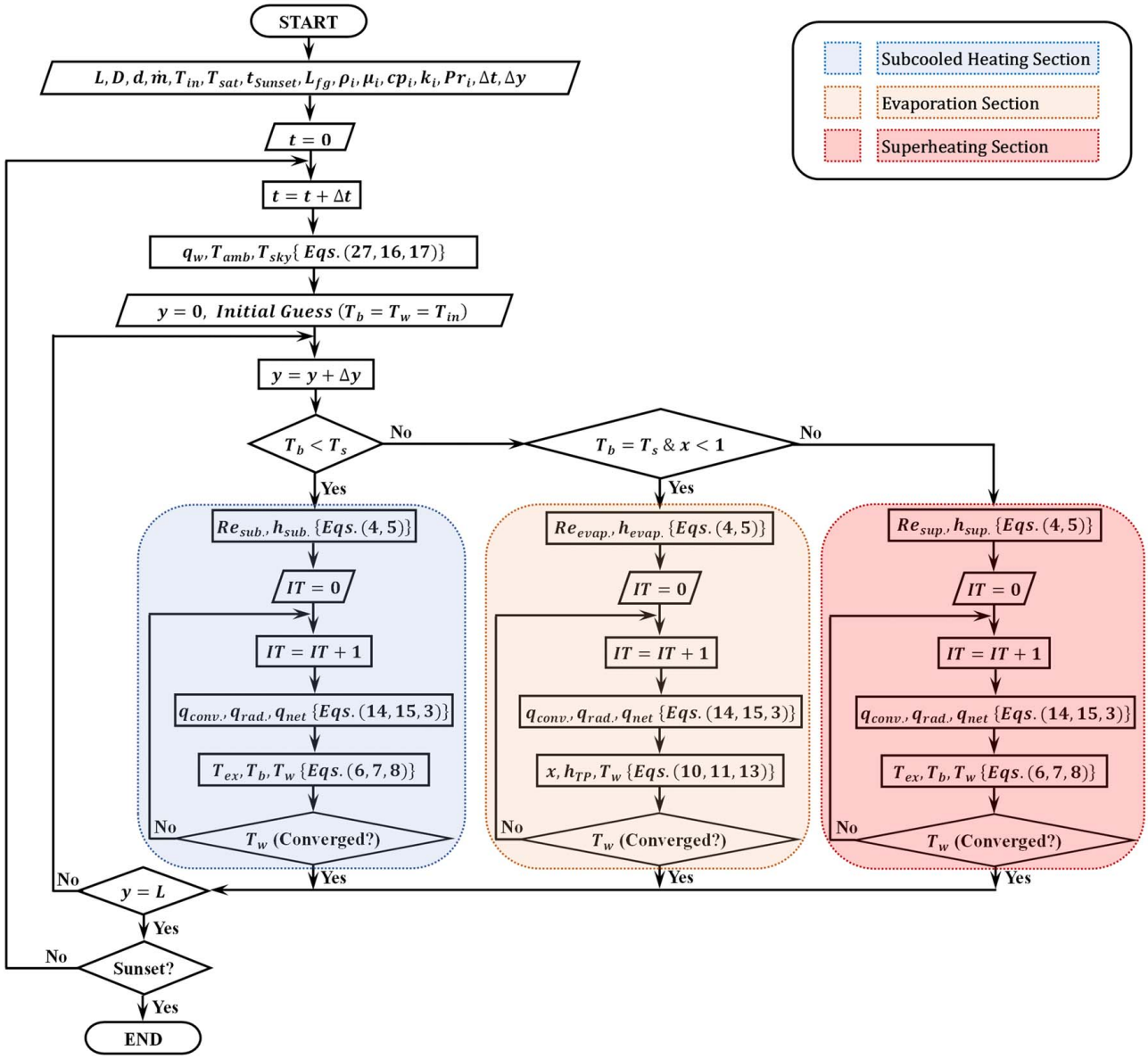

Fig. 10 Flowchart of the in-house code built for calculations

Next, the receiver geometry, receiver position, optical properties, and the design thermal losses are set. Hence, the receiver comprises four flat plates, each 23.8 m high and 16 m wide. Since this receiver has four sides, the optical performance simulation and heat flux distribution calculations are repeated for each side (north, east, south, and west). The receiver orientation azimuth is 0 deg based on the following convention (north = 0 deg, east = 90 deg, south = ±180 deg, west = −90 deg). As the tower does not tilt, the receiver orientation elevation is 0 deg, while its thermal absorptance percentage is 94%. Note that thermal losses due to convection and radiation are introduced as virtual zero values to carry out this simulation. However, these losses are separately and accurately calculated later in the developed MATLAB code. CFD packages can also evaluate convective and radiative heat losses on the absorbing tubes.

3.2 Numerical Solution. An in-house MATLAB code has been built to solve the current transient and one-dimensional problem numerically. First, the physical domain has been discretized into several cylindrically shaped longitudinal elements, as shown in Fig. 9. So, as demonstrated by the calculation flowchart in Fig. 10, the temporal variation in weather data is first computed using relevant data correlated with this purpose. After that, and for each time-step under consideration, an iterative solution is conducted to predict the bulk and wall temperatures and, hence, the corrected net heat gain based on the physical state of the HTF at each control volume of the tube. Convergence is measured in terms of the maximum change allowed in wall temperature during any iteration, where the quantitative maximum change allowed for the convergence check is 10^{-6}.

Table 2 Sensitivity of numerical solution to the size of the element adopted

$\Delta y\ (m)$	0.1	0.05	0.01	0.005	0.001	0.0005
$T_{b,\text{out}_{\max}}(K)$	643.51799	645.66424	648.35770	648.74097	649.01822	649.05682
Error %	–	0.334	0.417	0.059	0.043	0.006

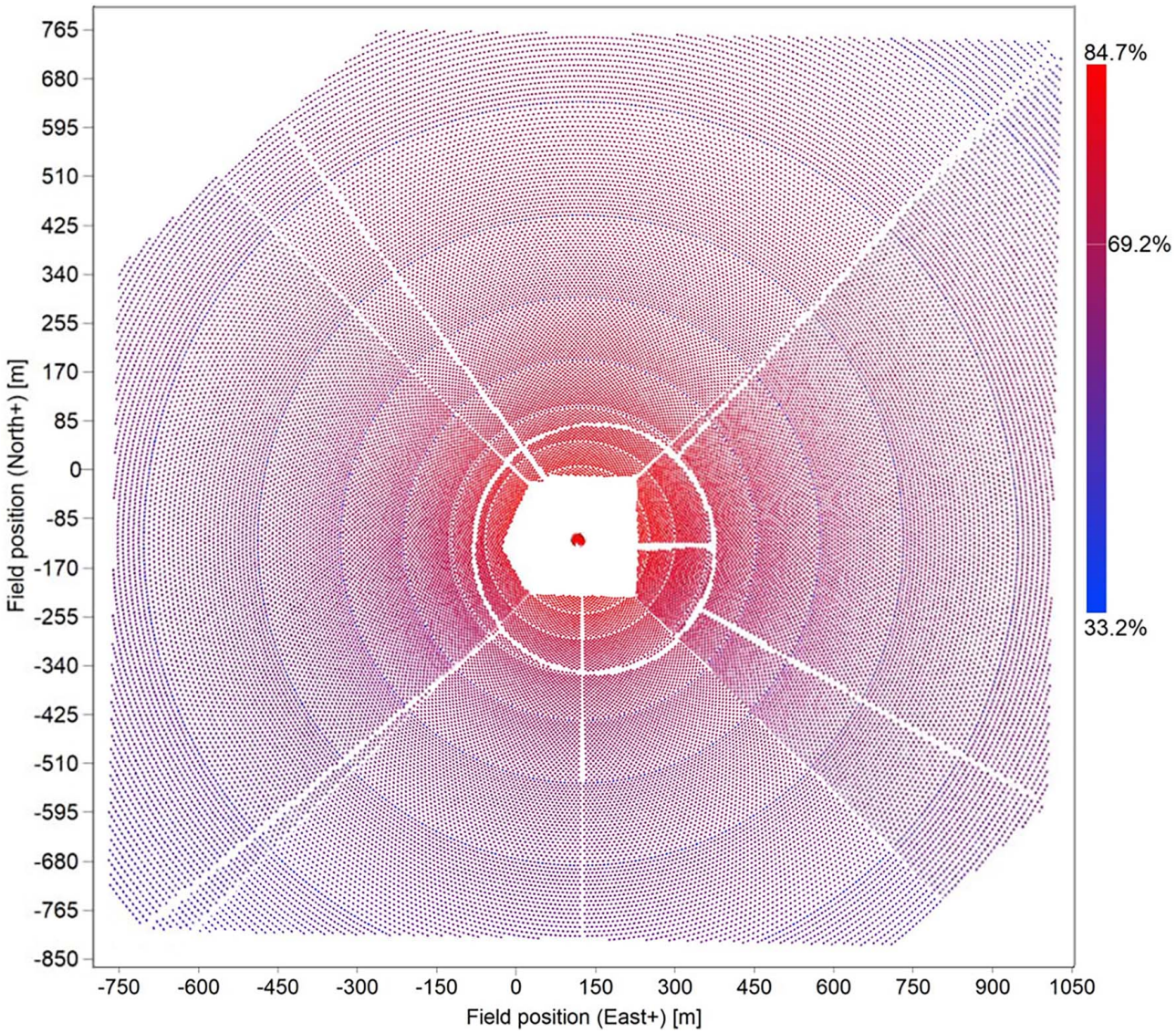

Fig. 11 Heliostats field layout of the Ivanpah I plant

The independence of the numerical solution from the element size adopted was checked by comparing the transient development of outlet bulk temperature during the daytime for six element sizes of $\Delta y = 0.1$, 0.05, 0.01, 0.005, 0.001, and 0.0005 m as Table 2 demonstrates. It has been found that the change in the data computed becomes quite marginal between the fifth and sixth mesh. Hence, an element size of 0.001 m has been used in the current analysis. As the heat gain processes have been assumed to be quasi-transient, only the transient influence due to temporal variation in solar heat gain has been considered. Hence, no time-step size influence is expected on the numerical solution accuracy. Therefore, a time-step size of $\Delta t = 5$ min has been adopted to enhance the temporal resolution of the results computed.

4 Results

4.1 Local and Temporal Distribution of Concentrated Solar Power. After executing the performance simulation by SOLARPILOT, the heliostat layout for each of the receiver's sides facing north, east, south, and west is generated, as shown in Fig. 11. Taking into consideration the heliostat dimensions mentioned before, the simulated total heliostat area of the northern, eastern, southern, and western fields is, respectively, 170,065.1, 159,831.2, 133,783.6, and 157,614.9 m^2, resulting in a total number of heliostats of 13,045, 12,260, 10,262, and 12,090 for each field, respectively. Also, the SOLARPILOT tool returns an estimation for the total price of the entire plant, which is approximately 100 million USD. The literature mentioned that the cost of heliostats is around 50% of the total price. That means heliostats cost around 50 million USD. The total amount of electric power generated annually by Ivanpah I is around 1000 GWh.

Table 3 summarizes the system's parametric results and tabulates the necessary parameters for the subsequent numerical investigation. The simulation is undertaken for the whole day of the 21st of June, from sunrise (5:00) until sunset (19:00). It also summarizes the solar power incident on the field facing each side of the receiver and the concentrated power incident on each side. The latest represents the amount of heat concentrated by heliostats and incident on the receiver minus the reflective heat. The convective and radiative heat losses are not considered as such losses as they cannot be precisely computed, as mentioned earlier. The data tabulated reveals that during the early times of the day, the western field played a significant role in amplifying the solar power incident on that field compared to other sides. This is attributed to the acute angle between the irradiance beam falling on the heliostat surface and

Table 3 Summary of parametric results for each of the receiver sides

		Simulation 1	Simulation 2	Simulation 3	Simulation 4	Simulation 5	Simulation 6	Simulation 7	Simulation 8	Simulation 9	Simulation 10	Simulation 11	Simulation 12	Simulation 13	Simulation 14	Simulation 15
Day hour		5	6	7	8	9	10	11	12	13	14	15	16	17	18	19
DNI (W/m^2)		17.1	524.5	749.4	739.7	844.2	887.3	911.9	910.4	956.6	941.3	910.5	834.1	637.3	558.0	193.7
Solar power incident on field (kW)	North	2904.2	89194.4	127,446.9	125,789.0	143,560.6	150,896.8	155,081.5	154,822.4	162,678.9	160,075.5	154,841.6	141,835.4	108,382.1	94,890.6	32,940.2
	East	2729.4	83,827.0	119,777.7	118,219.5	134,921.7	141,816.4	145,749.2	145,505.7	152,889.5	150,442.7	145,523.8	133,300.3	101,860.0	89,180.4	30,958.0
	South	2284.6	70,165.8	100,257.6	98,953.4	112,933.6	118,704.7	121,996.6	121,792.8	127,973.2	125,925.2	121,807. 9	111,576.4	85,260.0	74,646.8	25,912.8
	West	2691.6	82,664.6	118,116.8	116,580.2	133,050.8	139,849.9	143,728.2	143,488.1	150,769.5	148,356.6	143,505.9	131,451.9	100,447.6	87,943.8	30,528.7
Concentrated solar power incident on the receiver (kW)	North	589.8	38,495.8	66,367.4	71,650.2	86,840.4	95,069.5	100,156.8	100,657.4	104,407.1	99,797.3	92,216.4	78,967.2	53,849.6	33,510.6	12,605.5
	East	472.5	22,838.8	39,987.7	46,693.4	61,774.9	73,500.0	83,848.8	91,071.3	102,163.4	105,463.7	105,328.5	97,755.0	70,931.5	44,979.4	21,861.0
	South	405.8	38,244.8	60,662.6	59,603.9	66,973.7	69,608.7	71,281.5	71,177.1	74,899.5	74,329.6	72,929.3	67,835.5	50,254.1	31,311.3	16,713.2
	West	628.8	53,683.5	86,253.4	85,568.1	95,161.7	95,962.6	93,051.0	86,066.3	82,201.7	72,091.7	60,872.1	47,676.5	30,473.1	20,676.6	7312.9
Average incident flux (kW/m^2)	North	1.6	107.5	185.4	200.2	242.6	265.6	279.8	281.2	291.7	278.8	257.6	220.6	150.4	93.6	35.2
	East	1.3	63.8	111.7	130.4	172.6	205.3	234.2	254.4	285.4	294.6	294.3	273.1	198.2	125.7	61.1
	South	1.1	106.8	169.5	166.5	187.1	194.5	199.1	198.8	209.2	207.7	203.7	189.5	140.4	87.5	46.7
	West	1.8	150	241	239	265.9	268.1	260	240.4	229.6	201.4	170.1	133.2	85.1	57.8	20.4
Peak incident flux (kW/m^2)	North	18.4	1650.3	2953.8	3178.1	3790.4	4092	4272.4	4282.6	4460.6	4305.2	4030.2	3492.1	2322.7	1307.8	546
	East	18.2	1066.8	1950.4	2277	2979.5	3484.5	3879.2	4099.3	4475.4	4514.5	4431.4	4041.3	2755	1403.5	918
	South	12.2	1830.8	3133.4	3176.9	3607	3771.8	3870.8	3865.6	4061.9	4012.1	3902	3575	2490.4	1323	844.1
	West	13.3	1980.5	3448.1	3528.2	3982.9	4101.7	4081.3	3881.4	3805.5	3408.3	2916	2300.2	1441.5	884.8	329.8

the reflected beam during that period, compared to the eastern side, where the corresponding angle is too obtuse. Then, due to the sun's orbital motion up to solar noon, the concentrated solar power on the eastern side becomes more comparable to that on the western side. At the same time, it is maximum on the northern side and minimum on the southern one. During the afternoon, the role of the eastern side becomes, on the contrary, more dominant in concentrating solar rays compared to all other sides. This is again attributed to the effect of the irradiance incident angle, which is very acute on the eastern side and too obtuse on the western one.

To further demonstrate how the concentrated solar power on the receiver panels varies during the daytime, contours of the incident solar flux on each side have been tracked along the day hours, as Fig. 12 depicts. In general, the distributions illustrated are all in support of the parametric data summarized in Table 3. The heat flux distribution indicated that the heat intensity changes over the receiver panels are nonuniform because of several factors. First, the sun's position varies during the diurnal cycle, leading to changes in the angle of incident rays. Consequently, the pattern of the heat flux map is nonuniform. Second, the heliostat design controls the sunlight concentration process, leading to central hot spots or a pattern of multiple concentric rings with the peak incident flux found on the center of the receiver sides, as shown in all cases below. Furthermore, the sun image on the northern side of the receiver is tilted in the early morning. Then, it shifts counterclockwise as the sun's position changes over time due to the solar zenith angle effect. For the same reasons, similar observations can be spotted on the other sides of the receiver, but to a lesser extent. It is also observed that the intensity of concentrated irradiance reflected by the heliostat field onto the receiver panels varies significantly with time, as the temporal variation in DNI magnitudes and cosine efficiency determines it.

From an operational point of view, several potential operational problems can arise due to the uneven heat flux distribution on the receiver panels, such as thermal stresses, lower receiver efficiency, and heat transfer fluid issues. Hence, areas with high heat flux (hot spots) could initiate uneven thermal stresses and expansion for the receiver absorbing tubes. As a result, fatigue, warping, and cracks potentially occur. In turn, the areas on the solar panels receiving low heat flux may not be sufficiently heated, diminishing solar receiver efficiency. In addition, the nonuniform heat flux distribution can lead to nonuniform heat transfer fluid flow characteristics (uneven thermophysical properties within the HTF itself), which may negatively impact the hydrothermal performance of the targeted heating process.

As preceded, only the front half of the absorbing tube receives a solar beam reflected from heliostats. Furthermore, such incident solar power has an irradiance beam form that is not entirely effective over the whole tube wall [44] due to the curvature of the tube wall in the circumferential direction. Accordingly, the temporal profile of axisymmetric heat flux "equivalent to the real-world heat flux applied" for each side of the receiver can be computed using the corresponding average solar heat flux incident on that side as Fig. 13 demonstrates. It is worth mentioning that such profiles are helpful in two-dimensional CFD simulations and quasi-one-dimensional thermodynamic analysis. Furthermore, the comparison introduced in Fig. 13 shows that the temporal profile of the axisymmetric heat flux incident on each side of the receiver agrees well with relevant data found in the literature. The maximum solar power received over the entire day was reported on the northern side of the receiver, while it was minimal on the southern side. Such results agree well with the steady-state conditions analysis [21], which states that the maximum thermal load was detected on the northern side of the receiver for solar power tower plants installed in the northern hemisphere. Moreover, the heat flux on the eastern and western sides of the receiver shows that the simulation adequately captures the fact that the higher angle between the solar beam incident and the flux reflected generates less concentrated solar thermal energy on the receiver. In other words, at sunrise, the angle is quite large for the heliostats in the eastern field, whereas it is considerably smaller for the heliostats on the western

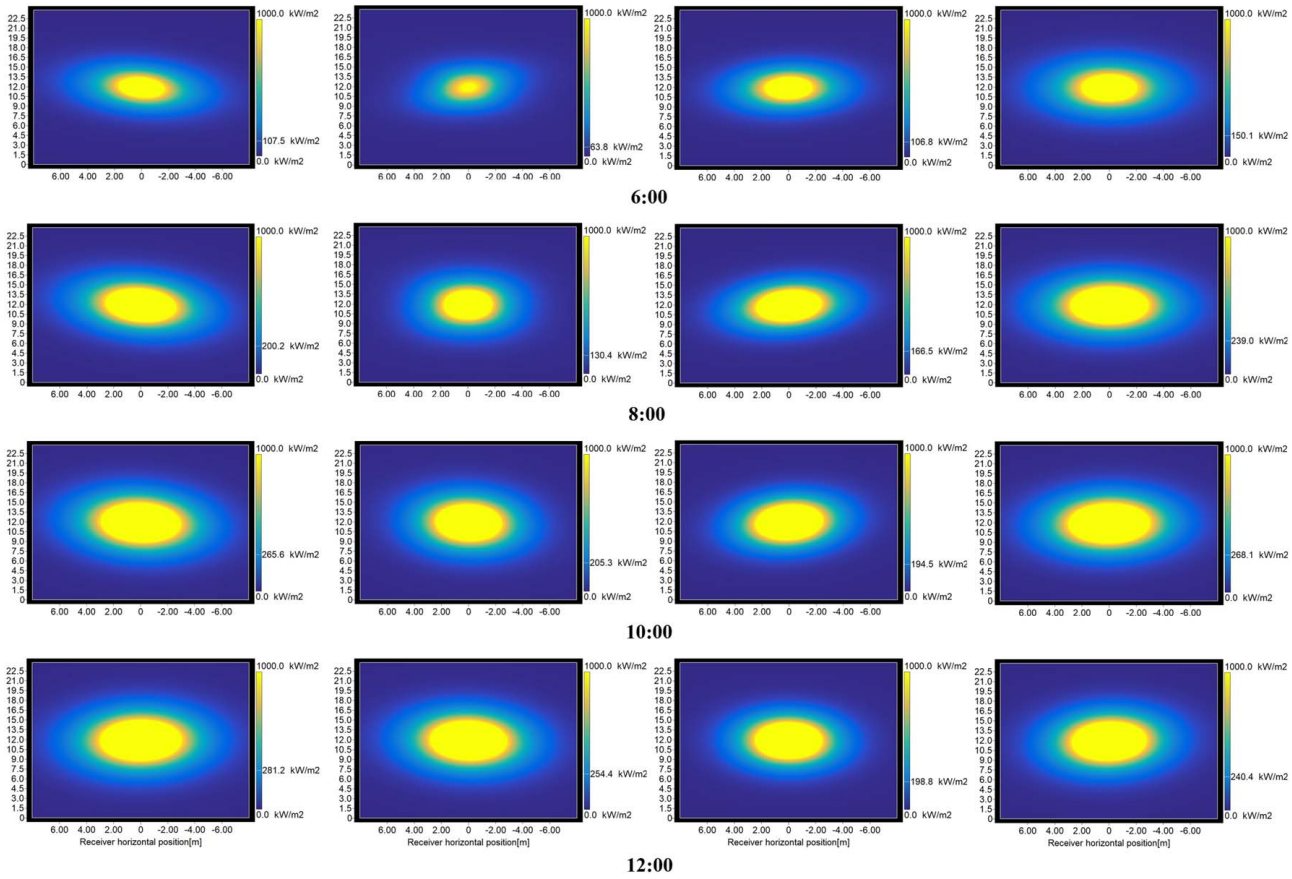

Fig. 12 Heat flux maps on the receiver sides facing "from left to right" north, east, south, and west

side. However, this scenario is overturned at sunset as the western heliostats deliver less concentrated solar power than the eastern ones due to the larger angle of incident irradiance.

Finally, to accurately capture the $q_{\text{Axisymmetric}}$ as a time-dependent variable that can be used in future analyses, a segment-based regression is set up for each profile on the four sides of the SPT receiver, as Eq. (27) states. Note that the sunrise represents the initial time, i.e., $t = 0$ s, for any future analysis that adopts the established correlations:

$$q_w = q_{Axisymmetric} = C_0 + C_1 t + C_2 t^2 + C_3 t^3 + C_4 t^4 + C_5 t^5 + C_6 t^6 \tag{27}$$

Consequently, a set of three-segment regression has been correlated to the temporal profiles estimated for the axisymmetric heat flux on each side of the receiver, as demonstrated in Fig. 14. It is worth mentioning that such correlations perfectly fit the data, where the minimal value of the coefficient of determination (R^2) 0.9989, 0.9994, 0.9985, and 0.9988 for the multisegment correlation generated for the receiver's northern, eastern, southern, and western sides, respectively. Note that the coefficients of the suggested regressions are all listed in Table 4.

4.2 Thermal Response to Temporal Variation in Atmospheric Conditions. The north-facing evaporator section of the Ivanpah I plant has been considered a case study to demonstrate the feasibility of the proposed solution procedure for predicting SPT receivers' performance. The temporal and local change of convective and radiative losses has been illustrated along with the net heat flux gained, as shown in Fig. 15. The overall losses due to convection and radiation are generally modest compared to the solar heat flux incident, slightly impacting the net heat gain. However, such losses are quite sensitive to the daytime and location along the tube due to their explicit reliance upon the tube wall temperature. This linkage is exhibited in Fig. 16 regarding the temporal and local distribution of wall and bulk temperatures. As the solar heat received changes over time, the wall temperature responds accordingly, resulting in variation in both the heat losses and bulk temperature. However, when HTF reaches the saturation condition, the phase-change phenomenon plays a key role in alleviating the wall temperature level to maintain a certain degree of temperature excess, i.e., $\Delta T_{\text{excess}} = T_w - T_{\text{sat}}$, resulting in a reduction in thermal losses. The evaporation region can be more distinguished by having a look at the temporal and local distribution of the inner heat transfer coefficient and the corresponding vapor fraction produced, as illustrated in Fig. 17. As the HTF flows through the subcooled region, i.e., no vapor has been generated yet, it receives heat in the sensible mechanism. Once the evaporation process starts, the heat transfer coefficient climbs rapidly with a gradual increase in the amount of HTF vapor generated. After the completion of the evaporation process, i.e., $x = 1$, the HTF is again heated sensibly as a superheated steam.

To have a better insight into the above-summarized phenomena, the local profiles of heat loss and gain, wall and bulk temperatures, and heat transfer coefficient with their corresponding vapor fraction have been plotted at certain times, as shown in Figs. 18–20, respectively. Figure 18 indicates that heat losses at sunrise decrease along the tube length due to the marginal amount of solar heat received, resulting in a negative amount of the corresponding net wall heat gain. This is apparent from the decreasing wall and bulk temperatures along the tube length, as shown in Fig. 19. As time elapses, the solar heat flux incident on the receiver starts rising to reach its peak by noon as Fig. 13 indicates. This increases heat loss and gain, leading to a substantial rise in wall and bulk temperatures. As wall temperature continues to increase over the tube length,

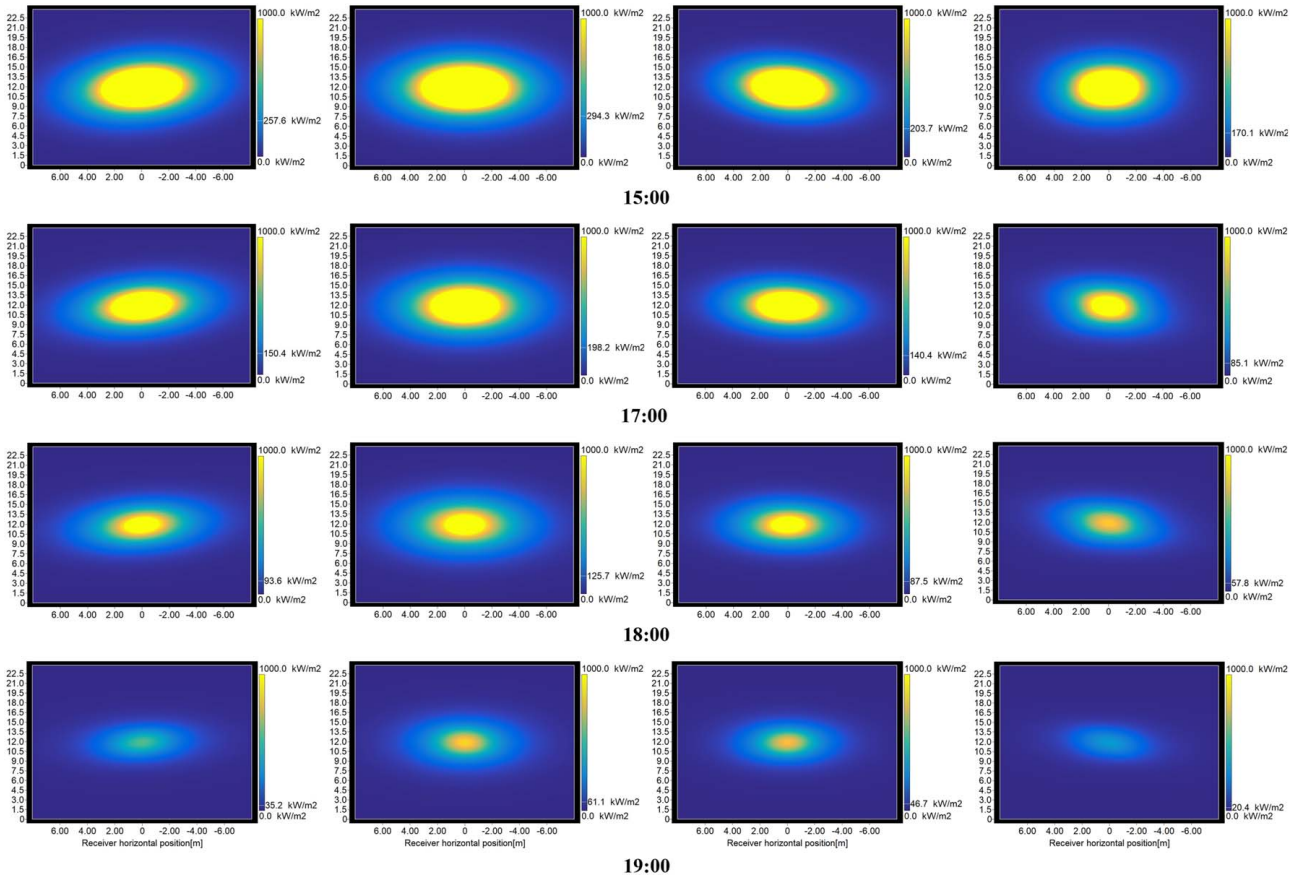

Fig. 12 ***Continued***

increased thermal losses occur, leading to a decreasing trend of net heat flux along the tube length. When solar irradiation becomes high enough, the HTF reaches the onset of nucleate boiling (ONB). In this region, HTF starts receiving heat in the latent form at a fixed value of bulk temperature, i.e., $T_b = T_{\text{sat}}$. This leads to a substantial enhancement in the heat transfer coefficient due to the boiling phenomenon involved, as Fig. 20 depicts, which justifies why the wall temperature stops climbing up and drops rapidly to maintain a constant degree of temperature excess, i.e., $T_w - T_{\text{sat}}$. Accordingly, a reduction in thermal losses leads to an increase in the net wall heat flux. Meanwhile, the vapor fraction grows due to the continuous steam generation along the tube length.

As solar irradiance varies from time to time, it is worth having a close look at the impact of its temporal change on the profiles obtained. When the solar heat increases, the tube wall temperature levels also rise, resulting in two consequences. The first is the increase in the amount of heat loss. The second is promoting the net wall heat gained by HTF, leading to higher rates of increase in the bulk temperature. That means a shorter length of the subcooled sensible heating region. Once boiling starts, the bulk temperature levels at different times are all unified at the saturation temperature corresponding to the system operating pressure. On the other hand, the wall temperature levels deviate from each other to different extents at different times. That results in various

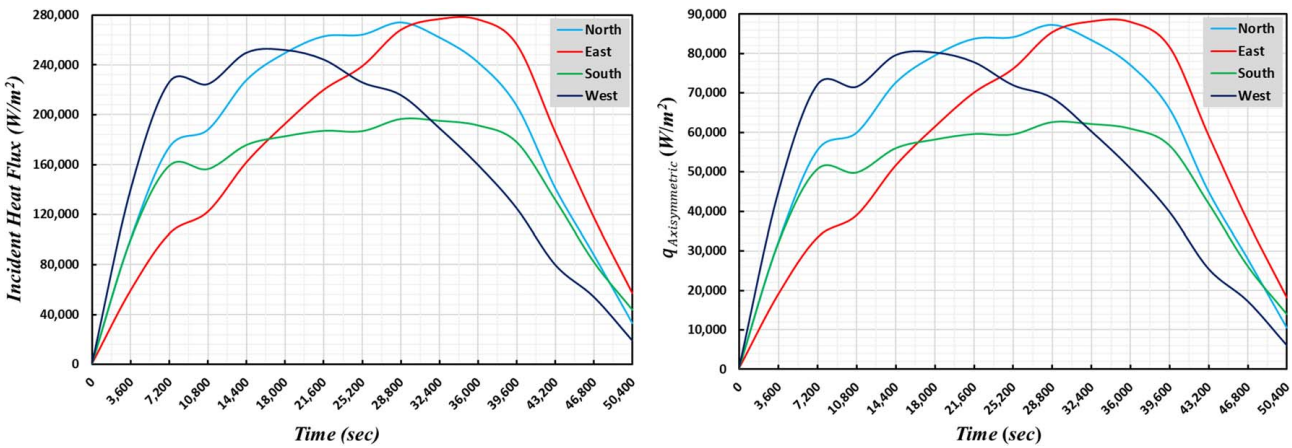

Fig. 13 Temporal variation of averaged (*a*) and axisymmetric heat flux (*b*) incident on each receiver side

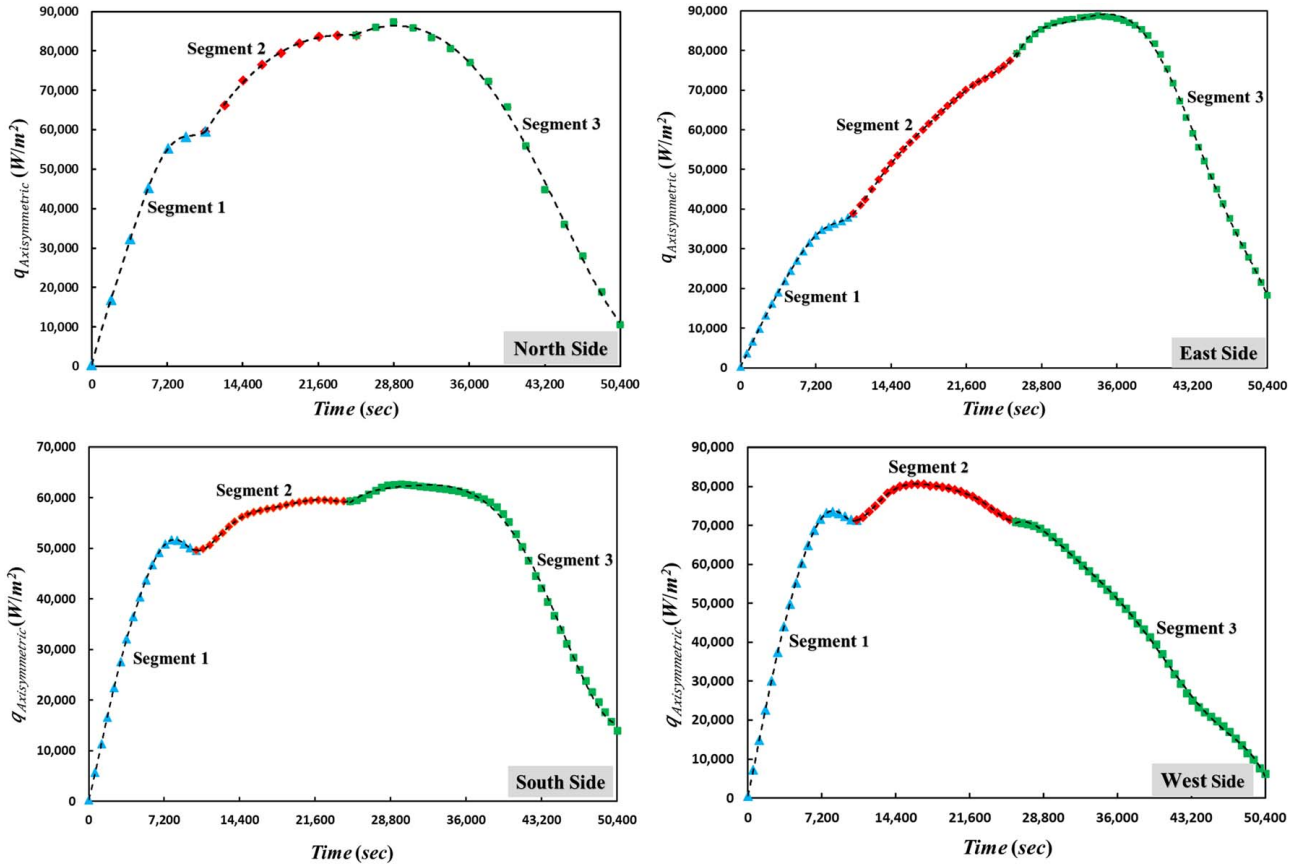

Fig. 14 $q_{Axisymmetric}$ versus time for the northern, eastern, southern, and western sides of the SPT receiver considered

degrees of temperature excess, such that the higher the solar heat is received, the higher the extent of temperature excess is. This, in turn, directly impacts the heat transfer coefficient levels and evaporation rate. As indicated in Fig. 20, the heat transfer coefficient levels up with time up to noontime in response to the corresponding increase in the net heat gained by the steam. Meanwhile, the vapor fraction grows at different rates depending on the net heat flux during a specific daytime. It is also worth noting that the length of the evaporation region differs from time to time depending on the heat supplied to the system and the corresponding rate of heat transfer, i.e., $h_{TP}(T_w - T_{sat})$. So, the higher the rate of heat transport, the shorter the evaporation region is. In other words, the higher the heat transfer coefficient and temperature excess are, the faster the evaporation process is. This is why the shortest tube length needed to generate 100% steam was at noon when the heat transfer coefficient and temperature excess were both at their peak. Consequently, the larger superheated section of the tube can be detected around midday when the solar heat received is at its peak.

To better explore the interlink between the key thermodynamic properties discussed above, they have been plotted together as thermal maps on various daytimes, as shown in Fig. 21. Four times in the first half of the day have only been considered as the rest are likely to give similar patterns but in a flipped-over trend with the progress in time. The net wall heat flux over the subcooled

Table 4 Segment-based $q_{Axisymmetric}$ correlation polynomials for the corresponding receiver sides

Coefficients	C_0	C_1	C_2	C_3	C_4	C_5	C_6
North side							
Segment 1	436.18	10.36	-12.63×10^{-4}	36.93×10^{-8}	-48.72×10^{-12}	19.88×10^{-16}	0
Segment 2	−15,457.69	9.98	-31.48×10^{-5}	29.85×10^{-10}	0	0	0
Segment 3	−291,425.43	52.86	-32.15×10^{-4}	10.46×10^{-8}	-17.48×10^{-13}	11.33×10^{-18}	0
East side							
Segment 1	353.9	5.01	47.26×10^{-5}	-24.06×10^{-8}	49.64×10^{-12}	-50.1×10^{-16}	18.49×10^{-20}
Segment 2	1,121,424.43	−400.5	0.059	-45.6×10^{-7}	19.3×10^{-11}	-42.88×10^{-16}	39.05×10^{-21}
Segment 3	−39,927,997.1	6556.6	−0.443	15.77×10^{-6}	-31.22×10^{-11}	32.52×10^{-16}	-13.94×10^{-21}
South side							
Segment 1	312.97	7.87	0.0019	-87.07×10^{-8}	16.12×10^{-11}	-14.61×10^{-15}	50.04×10^{-20}
Segment 2	1,699,216.86	−604.5	0.089	-69.35×10^{-7}	29.54×10^{-11}	-65.93×10^{-16}	60.34×10^{-21}
Segment 3	−11,624,266.85	1920.83	−0.129	45.81×10^{-7}	-89.45×10^{-12}	91.33×10^{-17}	-38.1×10^{-22}
West side							
Segment 1	518.78	11.51	19.15×10^{-4}	-89.35×10^{-8}	16.53×10^{-11}	-15.3×10^{-15}	53.45×10^{-20}
Segment 2	1,957,674.7	−685.9	0.1	-76.77×10^{-7}	32.2×10^{-11}	-70.71×10^{-16}	63.67×10^{-21}
Segment 3	−19,180,062.12	3202	−0.22	79.77×10^{-7}	-16.14×10^{-11}	17.25×10^{-16}	-76.08×10^{-22}

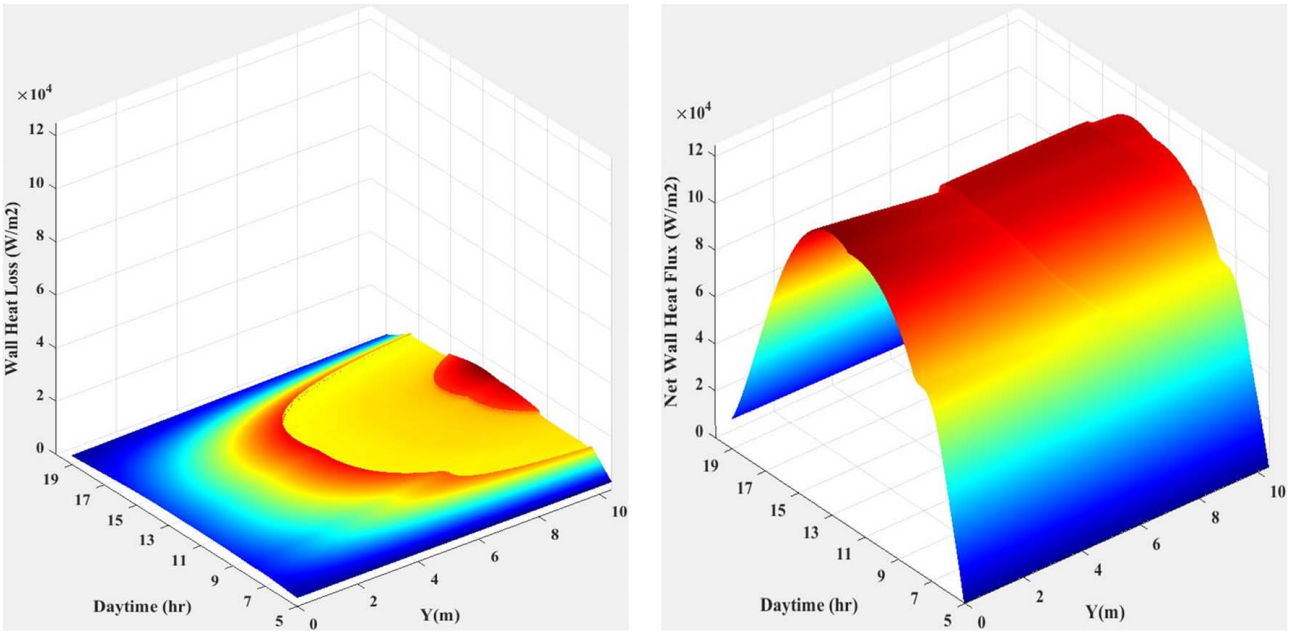

Fig. 15 Local and temporal distribution of the net wall heat loss (*a*) and gain (*b*)

region gradually decreases along the tube due to the continuous increase in wall temperature. That causes an increase in heat losses, as mentioned before. Next, the magnitude of net heat flux rapidly jumps once the phase-change phenomenon initiates. Such a jump results from the rapid rise in the heat transfer coefficient, almost one order of magnitude at the beginning of the evaporation region, with a noticeable reduction in wall temperature. During the evaporation process, the bulk temperature maintains its constant saturation condition. In contrast, the wall temperature first undergoes a sudden drop to respond to the dramatic increase of the heat transfer coefficient due to the boiling phenomenon and then climbs up slightly along the evaporation region. Consequently, the net wall heat flux first undergoes a sudden rise, then decreases slightly along the evaporation region due to the monotonic increase in thermal losses. Meanwhile, such a phase-change process involves a steady increase in the steam generated, as indicated by the linear climb of vapor fraction with the tube length. However, due to the insufficient solar thermal energy received at 7:00 and 9:00, such latent heating continues to the end of the tube, where no superheated steam is delivered. On the other hand, due to the higher rates of solar energy exerted at 11:00 and 13:00, the evaporation process completes, and superheated steam is generated. As the phase-change process ends, the heat transfer coefficient drops sharply, resulting in a sudden rise in the wall temperature. That causes a rapid drop in the net heat flux gained because of the sharp increase in thermal losses. In this superheating region, steam receives heat in a sensible form, allowing for a continuous rise of its bulk temperature.

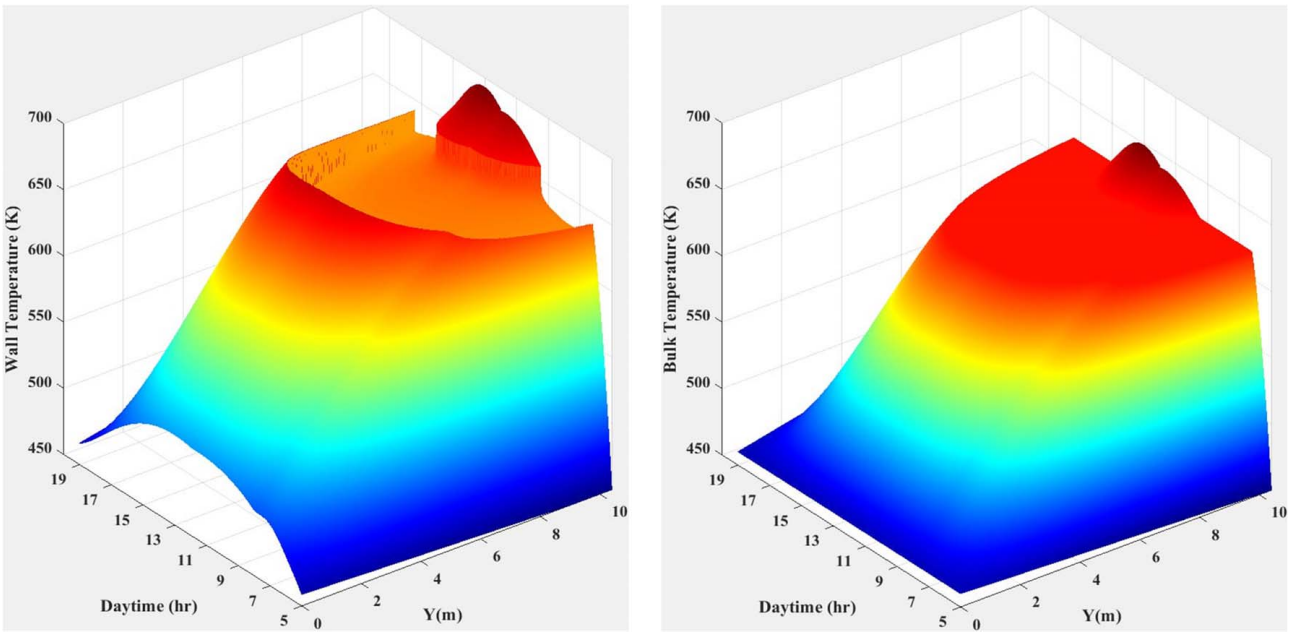

Fig. 16 Local and temporal distribution of the tube wall (*a*) and bulk temperature (*b*)

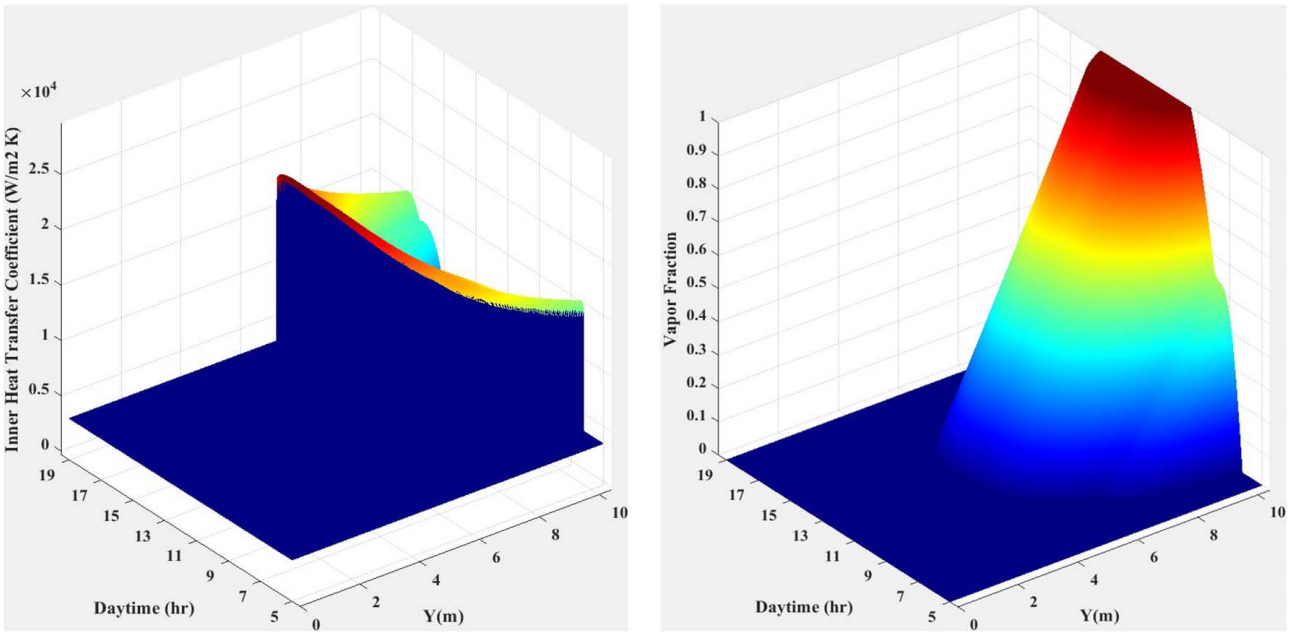

Fig. 17 Local and temporal distribution of the inner heat transfer coefficient (*a*) and vapor fraction (*b*)

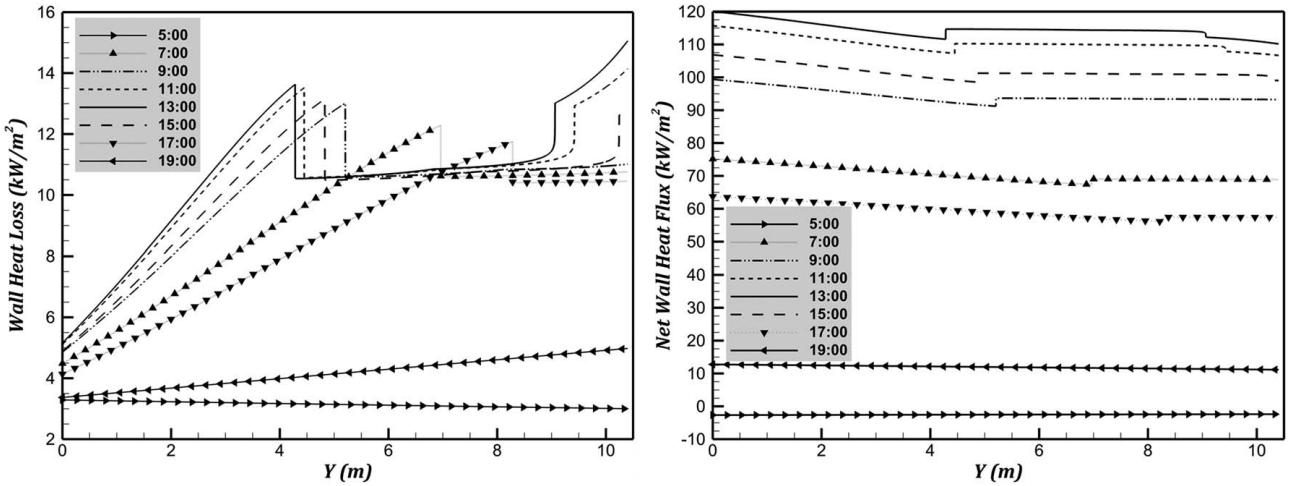

Fig. 18 Local profile of the wall heat loss (*a*) and net wall heat gain (*b*) at various day hours

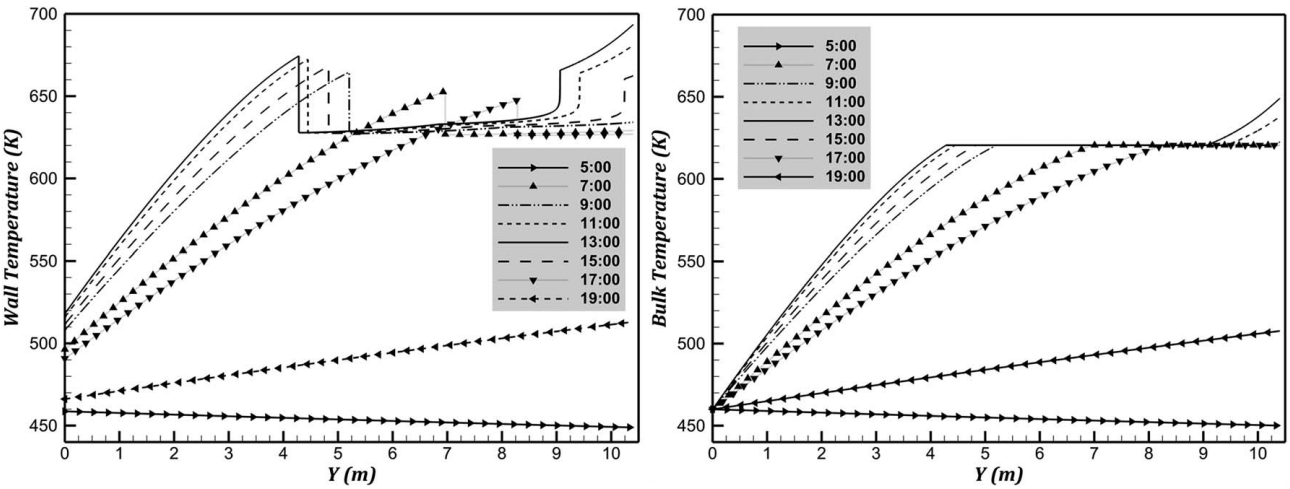

Fig. 19 Local profile of the wall (*a*) and bulk (*b*) temperatures at various day hours

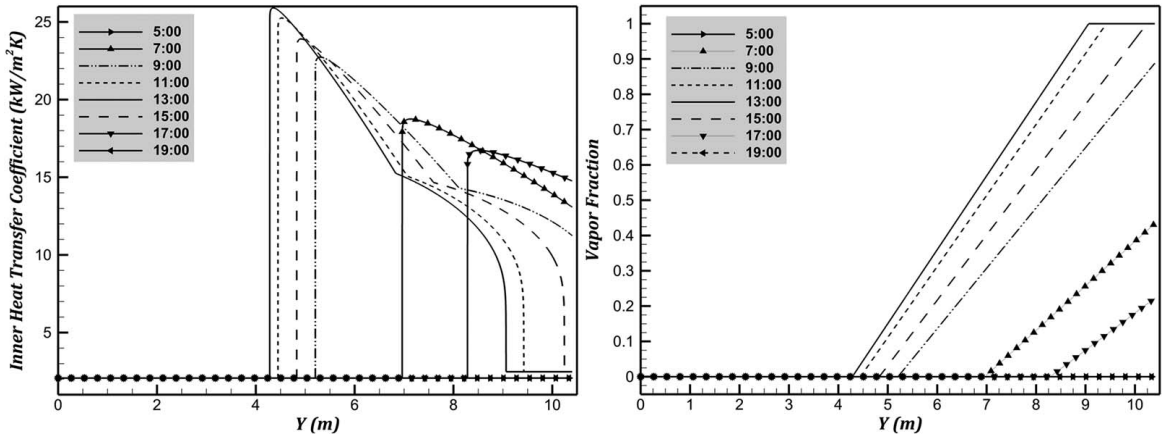

Fig. 20 Local profile of the inner heat transfer coefficient (*a*) and vapor fraction (*b*) at various day hours

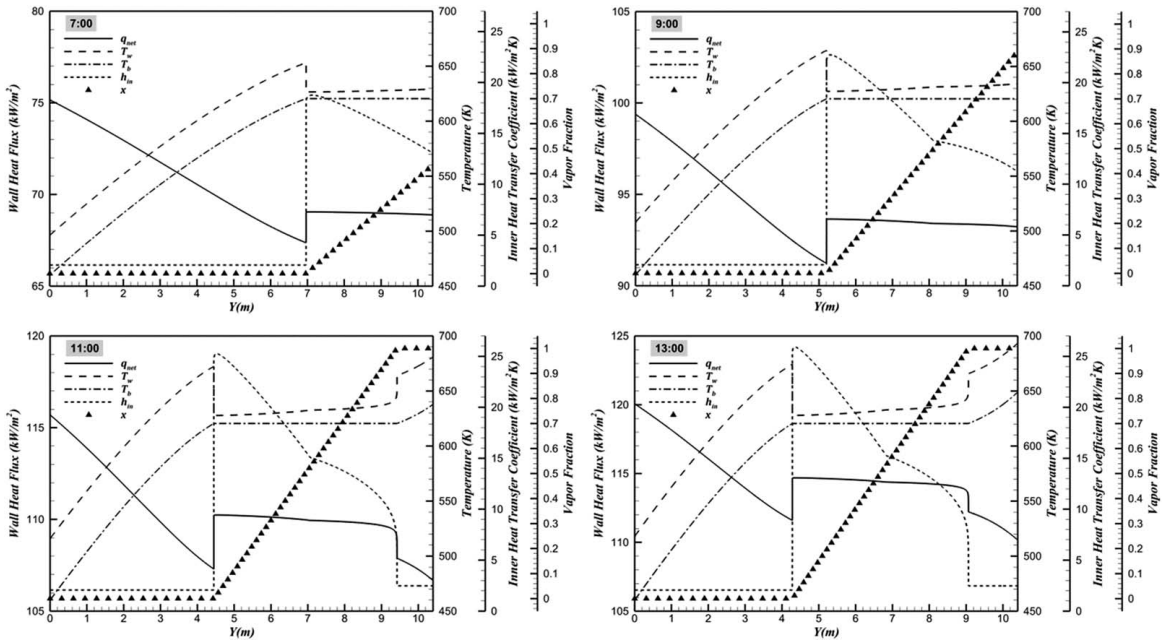

Fig. 21 Thermal characteristics map at various day hours

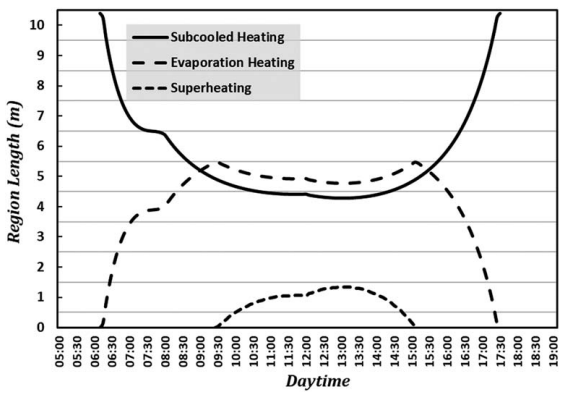

Fig. 22 Instantaneous variation of different heating regions evolved during the daytime

From an operational point of view, reaching the ONB at earlier times of the day, 7:00 and 9:00, requires a longer tube section, as the solar heat intensity applied is insufficient. Later, as solar intensity increases at 11:00 and 13:00, boiling starts earlier, and the ONB is realized with a shorter tube length. So, the higher the solar radiation intensity, the shorter the tube section required to reach the ONB. This fact can be better summarized in Fig. 22, which highlights the ONB inception locus on the tube with its corresponding length of evaporation region against daylight hours. Hence, in the early morning (6:00 am), reaching the ONB requires the subcooled HTF to be heated sensibly over the whole tube length, $L_{\text{Sub.}} = 10.4$ m. This means no evaporation is realized because of the deficiency in solar irradiance. As time progresses up to noon, the ONB can be realized with a shorter tube section once the solar irradiance is strong enough to generate steam, where the earliest ONB locus on the tube can be realized, $L_{\text{Sub.}} = 4.4$ m, when the maximum solar intensity takes place. In the meantime, the evaporation region starts prolonging to occupy the remaining length of the tube up to 5.5 m as long as the solar intensity is not sufficient to realize the superheating condition, either at 9:30 or 15:15. However, as the solar radiation gets stronger around midday, the evaporation region gets shorter and becomes $L_{\text{Evap.}} = 4.8$ m at 13:00. Once evaporation is completed, a superheating region emerges to occupy the rest of the tube whenever it exists. However, it is observed that the maximum length of the superheating region $L_{\text{Sup.}} = 1.34$ m is synchronized with the minimum lengths of the subcooled and evaporation regions at 13:05.

5 Conclusions

SPTs have a promising horizon and high potential to produce electricity based on solar thermal power, which fluctuates according to the location and time of day. Therefore, this research sets the foundation for analyzing weather conditions fluctuation as time-dependent inputs for external solar receivers. By doing so, it would be possible to carry out detailed CFD or simplified thermodynamic analyses to predict such plants' hydrothermal and mechanical characteristics. Taking Ivanpah I as a reference plant, the SOLARPILOT tool simulates the heliostat field layout and heat flux distribution on the receiver panels. A modified Gaussian distribution is introduced to apply an effective (normal) component of the concentrated thermal power over the tube circumference. A comprehensive thermodynamic analysis procedure is constructed and applied under real-world weather conditions to demonstrate its capability to handle such complicated computations thoroughly and cost-effectively. Following the established scheme, an in-house MATLAB code is developed to predict the instantaneous heat losses from a north-facing evaporator panel tube, along with its other thermal characteristics and the corresponding steam productivity. Overall, the current research paves the way for future CFD investigations with higher accuracy for external solar receivers. It also discloses the strong interlink between solar irradiance fluctuation and the resulting heat losses, steam productivity, and tube wall overheating, which helps ensure the reliability and longevity of such systems. Additional remarks can be concluded as follows:

- Compared to the proposed modified Gaussian distribution of solar heat flux, the uniform and basic Gaussian distributions employed previously in the literature result in about 57.1% overestimation of the total solar power received.
- Three-segment correlations are also established to perfectly fit the temporal profile of axisymmetric heat flux on each receiver side with up to 0.9985 minimal value of (R^2) for the generated multisegment correlations.
- Temporally, heat losses are directly proportional to solar irradiance intensity. They are also found to constantly increase either over the subcooled or superheated region, unlike the evaporation region, where they experience a noticeable drop at the threshold of the boiling process.
- The onset of nucleate boiling takes up to 2 h from sunrise to reach, with 70% of the tube length required to start evaporation, which lasts to the rest of the tube.
- Superheating can be established once solar intensity is strong enough around midday, occupying up to 12.9% of the evaporator tube length.

6 Future Considerations

Based on the current research findings, several knowledge aspects/gaps could be investigated/covered:

- Performing a sensitivity analysis could be beneficial to determine the key parameters affecting the thermal performance of solar receivers, such as solar irradiance, wind speed, and HTF mass flowrate.
- Detecting the hot spots on the receiver tube wall in advance would enable the designers of such plants to apply specific control/operation strategies to avoid thermal stresses and mechanical failure.
- Extending the current work to address all receiver sides (north, east, south, and west) of the evaporator and superheater sections would be useful in characterizing their individual contribution to steam productivity.
- Identifying the quality and quantity of steam produced from the receiver during the daytime would result in knowing the electric power expected to be generated by SPT plants.

Conflict of Interest

There are no conflicts of interest.

Data Availability Statement

The datasets generated and supporting the findings of this article are obtainable from the corresponding author upon reasonable request.

Nomenclature

d = Inner diameter (m)
g = Gravity acceleration (m/s^2)
h = Specific enthalpy (J/kg), convective heat transfer coefficient ($W/m^2 K$)
k = Thermal conductivity (W/m K)
q = Heat flux (W/m^2)
t = Time (s)
x = Vapor fraction
y = Distance in the y direction (m)
A = Area (m^2)
D = Outer diameter (m)
F = Fluid–solid combination factor
G = Mass flux ($kg/m^2 s$)
L = Tube length (m)
T = Temperature (K)
U = Velocity (m/s)
$\dot{m}$ = Mass flowrate (kg/s)
$q_{\text{Axisymmetric}}$ = Axisymmetric heat flux (W/m^2)
L_{fg} = Latent heat of vaporization (J/kg)
$\dot{Q}_{inc}$ = Total incident thermal power on the receiver surface (W)
Q_T = Concentrated solar power incident on the receiver (W)
BOLG = Boiling number
CO = Convective number
cp = Specific heat (J/kg K)
Gr = Grashof number
Pr = Prandtl number
Re = Reynolds number
Ri = Richardson number

Greek Symbols

α = Receiver surface reflectivity
β = Volume expansion coefficient (1/K)
ε = Emissivity
μ = Dynamic viscosity (Pa s)
ν = Kinematic viscosity (m^2/s)
ρ = Density (kg/m^3)
σ = Stefan–Boltzmann constant ($W/m^2 K^4$)

Subscripts

amb = Ambient
b = Bulk
cbd = Convection boiling dominant
conv = Convection
D = Along the tube diameter
ex = Section exit
for = Forced
i = Subcooled or superheated section
in = Section inlet, inner tube surface
j = Location index
l = Liquid
L = Along the tube length
n = Normal
nat = Natural
nbd = Nucleate boiling dominant
net = Net
out = Outer tube surface
r = Average
rad = Radiation
s = Surface
sky = Sky

t = Tangential
TP = Two-phase
v = Vapor
w = Wall
sat = Saturation

Abbreviations

CFD = Computational fluid dynamics
CSP = Concentrating solar power
DNI = Direct normal irradiance
DSG = Direct steam generation
HTF = Heat transfer fluid
ISEGS = Ivanpah Solar Electric Generating System
SPT = Solar power tower
NREL = National Renewable Energy Laboratory
NSRDB = National Solar Radiation Database
MIDC = Measurement and Instrumentation Data Center
ONB = Onset nucleate boiling

References

[1] Alhusseny, A., Al-Zurfi, N., Al-Aabidy, Q., Nasser, A., and Al- Madhhachi, H., 2024, "Response to the Design Conditions of a Tube-Bundle Thermal Energy Storage Unit With Paraffin-Copper Foam Composite as a Storage Medium," Int. J. Heat Mass Transf., **228**, p. 125679.
[2] Gupta, P. K., 1999, "Renewable Energy Sources - A Longway to Go in India," Renewable Energy, **16**(1-4), pp. 1216–1219.
[3] Abbott, D., 2010, "Keeping the Energy Debate Clean: How Do We Supply the World's Energy Needs?," Proc. IEEE, **98**(1), pp. 42–66.
[4] Tian, Y., and Zhao, C. Y., 2013, "A Review of Solar Collectors and Thermal Energy Storage in Solar Thermal Applications," Appl. Energy, **104**, pp. 538–553.
[5] Dascomb, J., 2009, *Low-Cost Concentrating Solar Collector for Steam Generation*, Florida State University, Tallahassee, FL.
[6] Mukesh, B. S., Mukhopadhyay, S., Mondal, A., and Chandra, L., 2022, "Numerical Design and Studies of Multipurpose Concentrated Solar Thermal Heating System," ASME J. Therm. Sci. Eng. Appl., **14**(7), p. 071011.
[7] Elmaddah, E., 2018, *An Assessment of Concentrating Solar Power for Egyptian Locations*, Auckland University of Technology, Auckland, New Zealand.
[8] Damerau, K., Williges, K., Patt, A. G., and Gauché, P., 2011, "Costs of Reducing Water Use of Concentrating Solar Power to Sustainable Levels: Scenarios for North Africa," Energy Policy, **39**(7), pp. 4391–4398.
[9] Kalogirou, S. A., 2013, "Solar Thermoelectric Power Generation in Cyprus: Selection of the Best System," Renewable Energy, **49**, pp. 278–281.
[10] Behar, O., Khellaf, A., and Mohammedi, K., 2013, "A Review of Studies on Central Receiver Solar Thermal Power Plants," Renewable Sustainable Energy Rev., **23**, pp. 12–39.
[11] Manente, G., Rech, S., and Lazzaretto, A., 2016, "Optimum Choice and Placement of Concentrating Solar Power Technologies in Integrated Solar Combined Cycle Systems," Renewable Energy, **96**, pp. 172–189.
[12] Shouman, E. R., and Khattab, N. M., 2015, "Future Economic of Concentrating Solar Power (CSP) for Electricity Generation in Egypt," Renewable Sustainable Energy Rev., **41**, pp. 1119–1127.
[13] Qaisrani, M. A., Fang, J., Jin, Y., Wan, Z., Tu, N., Khalid, M., Rahman, M. U., and Wei, J., 2019, "Thermal Losses Evaluation of an External Rectangular Receiver in a Windy Environment," Sol. Energy, **184**, pp. 281–291.
[14] Fang, J., Qaisrani, M. A., Tu, N., Wei, J., Wan, Z., Jin, Y., Khalid, M., and Ahmed, N., 2022, "Experiment and Numerical Analysis of Thermal Performance of a Billboard External Receiver," Energies, **15**(6), p. 2188.
[15] Mokhtar, M., Berger, M., Zahler, C., Krüger, D., Schenk, H., and Stieglitz, R., 2015, "Direct Steam Generation for Process Heat Using Fresnel Collectors," Int. J. Therm. Environ. Eng., **10**(1), pp. 3–9.
[16] Parzen, M., 2017, *Comparison of Heat Transfer Fluids (HTF) for Solar Tower Systems*, University of Applied Sciences Nuremberg, Germany.
[17] Phelan, P., Otanicar, T., Taylor, R., and Tyagi, H., 2013, "Trends and Opportunities in Direct-Absorption Solar Thermal Collectors," ASME J. Therm. Sci. Eng. Appl., **5**(2), p. 021003.
[18] Rodríguez-Sánchez, M. R., Soria-Verdugo, A., Almendros-Ibáñez, J. A., Acosta-Iborra, A., and Santana, D., 2014, "Thermal Design Guidelines of Solar Power Towers," Appl. Therm. Eng., **63**(1), pp. 428–438.
[19] Rodriguez-Sanchez, M. R., Sanchez-Gonzalez, A., Marugan-Cruz, C., and Santana, D., 2015, "Flow Patterns of External Solar Receivers," Sol. Energy, **122**, pp. 940–953.
[20] Liu, Y., Wang, W., Zhang, C., Li, T., and Zhao, X., 2024, "Improving the Heat Transfer Performance of the Tower Molten Salt Solar Receiver With the Novel Folded Flow Tubes," ASME J. Therm. Sci. Eng. Appl., **16**(2), p. 021003.
[21] Crespi, F., Toscani, A., Zani, P., Sánchez, D., Manzolini, G., and Max, ΔQ, 2018, "Effect of Passing Clouds on the Dynamic Performance of a CSP Tower Receiver With Molten Salt Heat Storage," Appl. Energy, **229**, pp. 224–235.
[22] Cagnoli, M., de la Calle, A., Pye, J., Savoldi, L., and Zanino, R., 2019, "A CFD-Supported Dynamic System-Level Model of a Sodium-Cooled Billboard-Type Receiver for Central Tower CSP Applications," Sol. Energy, **177**, pp. 576–594.
[23] NREL, "Power Tower Projects," Concentrating Solar Power Projects." https://solarpaces.nrel.gov/by-technology/power-tower.
[24] Qaisrani, M. A., Wei, J., Fang, J., Jin, Y., Wan, Z., and Khalid, M., 2019, "Heat Losses and Thermal Stresses of an External Cylindrical Water/Steam Solar Tower Receiver," Appl. Therm. Eng., **163**, p. 114241.
[25] Maytorena, V. M., and Hinojosa, J. F., 2019, "Three-Dimensional Numerical Study of Direct Steam Generation in Vertical Tubes Receiving Concentrated Solar Radiation," Int. J. Heat Mass Transf., **137**, pp. 413–433.
[26] NREL, "Jemalong Solar Thermal Station CSP Project," Concentrating Solar Power Projects. https://solarpaces.nrel.gov/project/jemalong-solar-thermal-station.
[27] Yang, X., Yang, X., Ding, J., Shao, Y., and Fan, H., 2012, "Numerical Simulation Study on the Heat Transfer Characteristics of the Tube Receiver of the Solar Thermal Power Tower," Appl. Energy, **90**(1), pp. 142–147.
[28] Maytorena, V. M., Hinojosa, J. F., Moreno, S., and Durán, R. L., 2023, "Enhancing the Thermal Performance of a Central Tower Tubular Solar Receiver With Direct Steam Generation by Using Internal Fins and Thicknesses Variation," ASME J. Heat Mass Transf., **145**(11), p. 111001.
[29] Maytorena, V. M., and Hinojosa, J. F., 2023, "Computational Analysis of Passive Strategies to Reduce Thermal Stresses in Vertical Tubular Solar Receivers for Safety Direct Steam Generation," Renewable Energy, **204**, pp. 605–616.
[30] Sánchez-González, A., Rodríguez-Sánchez, M. R., and Santana, D., 2022, "FluxSPT: Tool for Heliostat Field Aiming and Flux Mapping in Solar Power Tower Plants," AIP Conf. Proc, **2445**(1), p. 120020.
[31] Wagner, M. J., and Wendelin, T., 2018, "SolarPILOT: A Power Tower Solar Field Layout and Characterization Tool," Sol. Energy, **171**, pp. 185–196.
[32] Behar, O., Grange, B., and Flamant, G., 2020, "Design and Performance of a Modular Combined Cycle Solar Power Plant Using the Fluidized Particle Solar Receiver Technology," Energy Convers. Manage., **220**, p. 113108.
[33] Martinek, J., Jape, S., and Turchi, C. S., 2021, "Evaluation of External Tubular Configurations for a High-Temperature Chloride Molten Salt Solar Receiver Operating Above 700 °C," Sol. Energy, **222**, pp. 115–128.
[34] Khatti, S. S., Jeter, S., and Al-Ansary, H., 2021, "Preliminary Techno-Economic Optimization of 1.3 MWe Particle Heating Receiver Based CSP Power Tower Plant for the MENA Region," Proceedings of the ASME 15th International Conference on Energy Sustainability (ES2021), Virtual Online, June 16–18, p. V001T02A016-1–8.
[35] Gamil, A., Li, P., and Khammash, A. L., 2023, "Modeling and Analysis of a Relocatable Solar Power Tower for Pressurized Water Heating and Storage Providing Low to Medium Temperature Industrial Process Heat," Energy Convers. Manage., **296**, p. 117698.
[36] NREL, "UNLV Solar Calendars," Measurement and Instrumentation Data Center (MIDC). https://midcdmz.nrel.gov/apps/cal.pl?site=UNLV.
[37] NREL, "The National Renewable Energy Laboratory (NREL)," https://www.nrel.gov/.
[38] Plotkin, A. R., Toupin, K. M., Gillum, C. B., Rancatore, R. J., Yang, T., and Mier, D., 2011, ASME Conference Proceedings, **POWER2011**(2), pp. 523–529.
[39] Kandlikar, S. G., 1998, "Boiling Heat Transfer With Binary Mixtures: Part II—Flow Boiling in Plain Tubes," ASME J. Heat Transf., **120**(2), pp. 388–394.
[40] Göksu, T. T., 2024, "Energy, Exergy Analysis, and RSM Modeling of Different Designed Twisted Tapes in Placed PV/T Systems," Energy, **304**, p. 132041.
[41] Yellowhair, J., Ho, C. K., Ortega, J. D., Christian, J. M., and Andraka, C. E., 2015, "Testing and Optical Modeling of Novel Concentrating Solar Receiver Geometries to Increase Light Trapping and Effective Solar Absorptance," SPIE Optics + Photonics for Sustainable Energy, San Diego, CA, Aug. 9–13, vol. 9559, p. 95590A.
[42] Bergman, T. L., Lavine, A. S., Incropera, F. P., and Dewitt, D. P., 2011, *Fundamentals of Heat and Mass Transfer*, 7th ed, John Wiley & Sons, Inc, Hoboken, NJ.
[43] Al-Arabi, M., and Khamis, M., 1982, "Natural Convection Heat Transfer From Inclined Cylinders," Int. J. Heat Mass Transf., **25**(1), pp. 3–15.
[44] Boerema, N., Morrison, G., Taylor, R., and Rosengarten, G., 2013, "High Temperature Solar Thermal Central-Receiver Billboard Design," Sol. Energy, **97**, pp. 356–368.
[45] Liao, Z., Li, X., Xu, C., Chang, C., and Wang, Z., 2014, "Allowable Flux Density on a Solar Central Receiver," Renewable Energy, **62**, pp. 747–753.
[46] Mahan, J. R., 2019, *The Monte Carlo Ray-Trace Method in Radiation Heat Transfer and Applied Optics*, John Wiley & Sons Ltd. and ASME Press, New York.
[47] NREL, "NSRDB: National Solar Radiation Database," https://nsrdb.nrel.gov/.
[48] Wagner, M. J., 2008, "Simulation and Predictive Performance Modeling of Utility-Scale Central Receiver System Power Plants," Masters Thesis, University of Wisconsin–Madison, Madison, WI.
[49] Sullivan, R., and Abplanalp, J., 2015, Visibility and Visual Characteristics of the Ivanpah Solar Electic Generating System Power Tower Facility, Argonne National Laboratory, Argonne, WI.